Shallow water equations with binary porosity and their application to urban flooding

Giada Varra, Res., Ph. D., Dept. of Engrg., Parthenope Univ., Centro Direzionale di Napoli – Is. C4, 80143 Napoli, Italy. E-mail: giada.varra@uniparthenope.it

Luca Cozzolino, Ass. Prof., Ph. D., Dept. of Engrg., Parthenope Univ., Centro Direzionale di Napoli – Is. C4, 80143 Napoli, Italy. E-mail: luca.cozzolino@uniparthenope.it

Renata Della Morte, Full Prof., Ph. D., Dept. of Engrg., Parthenope Univ., Centro Direzionale di Napoli – Is. C4, 80143 Napoli, Italy. E-mail: renata.dellamorte@uniparthenope.it

Sandra Soares-Frazão, Full. Prof., Ph. D., Inst. Mech. Mat. & Civ. Engrg. Place du Levant 1, 1348 Louvain-la-Neuve, Belgium. E-mail: sandra.soares-frazao@uclouvain.be

Abstract

Climate change and urbanization, among various factors, are expected to exacerbate the risk of flood disasters in urban areas. This prompts the construction of appropriate modelling tools capable of addressing full-scale urban floods for hazard and risk assessment. In this view, sub-grid porosity models based on the classic Shallow water Equations (SWE) appear to be a promising approach for full-scale applications in urban environments with reduced computational cost respect to classic SWE models on high-resolution grids. The present work focuses on the recently proposed two-dimensional (2-d) Binary Single Porosity (BSP) model, which is a porosity flooding model written in differential form and based on the use of a binary indicator function to locate obstacles and buildings. Several applications (synthetic, experimental, and real-world cases) show that (i) the BSP results tend to the classic SWE solution for sufficiently refined mesh and that (ii) the BSP model can be successfully applied to realistic conditions with complicated terrain and obstacle distribution on coarser grids. Clearly, the adoption of medium/coarse grids makes the BSP model inherently less accurate than the classic SWE model on high-resolution grids, but the corresponding reduction of computational cost makes the use of the BSP model promising in full-scale urban flood applications when (i) multiple *simulations are needed to perform stochastic or scenario analysis, (ii) no detailed information of local flow characteristics is required, and/or (iii) for complementing classic SWE models in a nesting cascade.*

Subject headings*:* Shallow water Equations; Porous Shallow water Equations; Spatially distributed porosity field; Urban flooding; Differential equations.

Corresponding author: Luca Cozzolino

E-mail address: luca.cozzolino@uniparthenope.it

Address: Dipartimento di Ingegneria, Università degli Studi di Napoli Parthenope, Isola C4, 80143 Napoli (Italy)

Phone: +390815476723

"*As porous as this stone is the architecture. Building and action interpenetrate in the courtyards, arcades, and stairways*". W. Benjamin and A. Lacis, *Neapel*. Frankfurter Zeitung, August 19th, 1925.

1. Introduction

Increasing anthropogenic factors such as rapid urbanisation and predictions about global climate change (IPCC 2022) are expected to increase urban flood risk. This risk is not only associated with loss of lives and properties (Gou et al. 2024), but also with stress and mental health issues (Cheema et al. 2022), spreading of infectious diseases (Paterson et al. 2018), and social inequities (Sanders et al. 2023). In this context, flood inundation numerical models are a well-established approach for supporting flood risk management initiatives, thanks to the ability to predict the spatiotemporal distribution of flood depths and velocities (Sanders and Schubert 2019).

Two-dimensional (2-d) shallow water equations (SWE) models are the state-of-the-art for the simulation of flood inundation processes and for the assessment of related flood hazard and risk levels (Costabile and Macchione 2015, Horváth et al. 2019, Schubert and Sanders 2012). For achieving accurate hydrodynamic predictions in urban areas, it is essential to produce very refined computational meshes (Mark et al. 2004, Soares-Frazão and Zech 2008) that capture the intricate network of narrow streets, buildings, and infrastructures of complex urban environments (Guinot et al. 2017, Zhang et al. 2023). However, the solution of the classic SWE model on high-resolution grids may result in excessively time-consuming simulations, limiting their potential to consider multiple scenarios and rapid forecasting.

To reach a trade-off between high-resolution flood modelling and computational efficiency, several strategies have been pursued in recent years. Besides the implementation of parallel computing techniques (Sanders and Schubert 2019, Vacondio et al. 2017), the reduction of computation burden can be achieved by resorting to a macroscopic modelling approach, where obstacles and streets are merged in medium/coarse-resolution cells and artificial porosity parameters are used to describe the underlying urban geometry. In this class of sub-grid shallow water models, called porosity-based models (Guinot and Soares-Frazão 2006, Sanders et al. 2008, Dewals et al. 2021), the porosity represents the fraction of areal (storage porosity) or linear space (convective porosity) that is free from blocking elements (buildings, walls, bridge piles, and trees), allowing the water propagation within the urban area. For a recent review on the topic, the reader is addressed to the work by Dewals et al. (2021). When simulating urban inundations with porosity models, one of the main goals is to find a balance between the computational cost reduction and the grid spatial resolution, since the adoption of relatively medium/coarse-size grids inevitably affects the quality of the flow field representation within built-up areas (Ferrari and Viero 2020).

Among the porosity models, a pioneer formulation is the differential Single Porosity (SP) model by Guinot and Soares-Frazão (2006). The SP model is obtained by space-averaging the SWE model over a Representative Elementary Area (REA) that is large enough to devise a stable and conceptually feasible averaging process (Velickovic 2012), following the same approach used to obtain the porous media equation by space averaging the Navier-Stokes equations (Whitaker 1969, 1999). In the SP model, the urban fabric geometry is described using the porosity $\varphi(x,y) \in [0, 1]$, which represents the REA fraction that is free from obstacles. Due to the irregular structure of urban fabrics, convergence of the space averaging operator is obtained only on REAs spanning many city blocks, leading to extreme smoothing of the averaged geometric and flow variables (Guinot 2012, Bruwier et al. 2014). This implies that uniform porosity $\varphi(x,y)$ is often assumed within the urban area, making the SP model application problematic when the description of the urban inner structure is required. Of course, the use of a numerical discretisation with elements finer than the REA is possible in SP computational schemes (Guinot and Soares-Frazão 2006, Petaccia et al. 2010, Guinot 2012, Velickovic et al. 2010, 2017), but the grid refinement does not compensate the loss of geometric information due to the REA space averaging and the adoption of uniform porosity.

In contrast with the differential SP approach, flooding models in integral form have been proposed in the literature (Sanders et al. 2008, Chen et al. 2012). In these models, the complex structure of urban environments is represented by a binary indicator function $I(x,y)$, which takes the value 1 in the points (x,y) of the domain that allow flood storage and conveyance and the value 0 in the points (x,y) inside buildings and obstacles. In the corresponding numerical schemes, local porosity values can be assigned to the computational cell and its interfaces after identification of the buildings contained therein (Sanders et al. 2008, Chen et al. 2012, Guinot et al 2017, Bruwier et al. 2017). Despite its main advantage, i.e., the definition of the porosity at the cell level, the integral form makes it difficult to study the model's mathematical structure (Guinot 2017) and define the interaction terms between flow and blocking elements. Moreover, integral model discretizations may lack an adequate dissipative mechanism representing the loss of flow energy through the urban fabric. Empirical coefficients, mainly dependent on the case study at hand, have been introduced in the literature to cope with this issue (Guinot et al. 2017).

In the present study, we focus on the Binary Single Porosity (BSP) shallow water model (Varra et al. 2020), which has recently emerged as a theoretical connection between the differential SP model and the integral SWE model by Sanders et al. (2008). The BSP model can be regarded as a special case of the SP model where the porosity $\varphi(x,y)$ reduces to the binary indicator function $I(x,y)$. For this reason, the BSP model retains the mathematical structure of the SP model (hyperbolicity, rotation and translation invariance, wave celerity), allowing to exploit the theory by Dal Maso et al (1995) for the definition of the non-conservative products representing the interaction between flow and structures. Like the integral porosity model, the BSP model is not based on space-averaging of the SWE model on an REA. This allows its use independent of the existence of an REA, supplying a sounding theoretical framework to those SP applications (Velickovic et al. 2017, Özgen et al. 2017, Soares-Frazão et al. 2018, Ferrari and Viero 2020, Nash et al. 2014) where the porosity varies from cell to cell according to the underlying urban geometry. A distinct advantage of the BSP model over the integral SWE models resides in its differential form, which simplifies the mathematical study and allows the use of classic numerical machinery for the approximation of the corresponding solutions (Varra et al. 2020). Existing porous SWE differential models where a distinction is made between storage and convective porosities, like the ones by Guinot et al. (2017)

and Bruwier et al. (2017), are not physically consistent and do not share the good properties of the BSP model, i.e., translational invariance, rotational invariance, and wave celerities coinciding with those of the classic SWE model (Varra et al. 2020, Dewals et al. 2021).

Despite the availability of theoretical results (Varra et al. 2020, 2023, Jung 2022), the consistency between the SWE and the BSP mathematical models and the ability of the BSP model to represent the urban fabric geometrical characteristics in real-world applications have not been assessed so far. In addition, the capabilities of the BSP model to simulate full-scale flood phenomena have not been tested against real-world events in urban environments. With these objectives in mind, we present an extended version of the BSP model by Varra et al. (2020) obtained by introducing the terms corresponding to variable bed elevation and bed friction (Varra 2021). The approximate solution of the improved BSP model is tackled with a first-order Finite Volume (FV) method on triangular unstructured grids where an SP Riemann problem is solved at the interface between cells. A novel two-step reconstruction of the conserved variables inspired by Audusse et al. (2004) and Varra et al. (2023) is used to treat the non-conservative products representing the interaction of the flow with the variable bed elevation and the obstacles. This reconstruction allows the introduction of localized energy losses at the interface between cells and the satisfaction of the well-balancing property, ruling out the nonphysical alternatives when multiple exact solutions of the interface SP Riemann problem are possible.

The paper is organized as follows. In Section 2, the 2-d Binary Single Porosity (BSP) shallow water model by Varra et al. (2020) is complemented with the introduction of bed elevation variations and bed friction, and the corresponding 2-d FV scheme is introduced. In Section 3, the BSP model properties are characterised through the thorough examination of a synthetic dam-break case study. In Section 4, the BSP model is validated using laboratory and real-world test cases from current literature, discussing the quality of the numerical results in terms of water depths and velocities, and assessing the computational time reduction with respect to the SWE model on refined grids. Concluding outlooks are finally presented in Section 5.

2. Binary Single Porosity model

In the present Section, the BSP model by Varra et al. (2020) is enhanced to consider variable bed elevation and friction, and its connection with the original SP model by Guinot and Soares-Frazão (2006) is presented. Subsequently, a first-order accurate FV scheme on triangular unstructured grid for the approximate solution of the BSP model is proposed.

2.1 Governing equations

The original 2-d SP model (Guinot and Soares-Frazão 2006, Velickovic 2012) can be written as

$$\text{(1)}\quad \frac{\partial \varphi \mathbf{U}}{\partial t}+\frac{\partial \varphi \mathbf{F}(\mathbf{U})}{\partial x}+\frac{\partial \varphi \mathbf{G}(\mathbf{U})}{\partial y}+\mathbf{H}_x(\mathbf{U})\frac{\partial \varphi}{\partial x}+\mathbf{H}_y(\mathbf{U})\frac{\partial \varphi}{\partial y}+\varphi \mathbf{B}_x(\mathbf{U})\frac{\partial z}{\partial x}+\varphi \mathbf{B}_y(\mathbf{U})\frac{\partial z}{\partial y}=\varphi \mathbf{S}_f(\mathbf{U}),$$

where t is the time, x and y are the horizontal coordinated axes of a fixed reference framework, $z(x,y)$ is the bed elevation, and $\varphi(x, y) \in [0, 1]$ is a storage porosity defined as the fraction of REA that is free from obstacles. The vector symbols in Eq. (1) are defined as

$$\text{(2)}\quad \begin{array}{l} \mathbf{U}=\begin{pmatrix} h & hu & hv \end{pmatrix}^T \\ \mathbf{F}(\mathbf{U})=\begin{pmatrix} hu & 0.5gh^2+hu^2 & huv \end{pmatrix}^T \quad \mathbf{G}(\mathbf{U})=\begin{pmatrix} hv & huv & 0.5gh^2+hv^2 \end{pmatrix}^T \\ \mathbf{H}_x(\mathbf{U})=\begin{pmatrix} 0 & -0.5gh^2 & 0 \end{pmatrix}^T \quad \mathbf{H}_y(\mathbf{U})=\begin{pmatrix} 0 & 0 & -0.5gh^2 \end{pmatrix}^T \\ \mathbf{B}_x(\mathbf{U})=\begin{pmatrix} 0 & gh & 0 \end{pmatrix}^T \quad \mathbf{B}_y(\mathbf{U})=\begin{pmatrix} 0 & 0 & gh \end{pmatrix}^T \\ \mathbf{S}_f(\mathbf{U})=\begin{pmatrix} 0 & -ghS_{f,x} & -ghS_{f,y} \end{pmatrix}^T. \end{array}$$

In Eqs. (1)-(2), $\mathbf{U}$ is the vector of the conserved hydrodynamic variables, where $h(x, y, t)$ is the flow depth, while $u(x, y, t)$ and $v(x, y, t)$ are the vertically averaged components of the flow velocity along x and y, respectively. Since the SP mathematical model is obtained after space-averaging of the

SWE model, the flow variables (h, u, and v) and the geometric variables (φ and z) in the point (x, y) must be intended as space averages in a REA centred in (x, y) (Velickovic 2012).

The meaning of the other symbols is the following: T is the matrix transpose; g is the gravity acceleration; $\mathbf{F}(\mathbf{U})$ and $\mathbf{G}(\mathbf{U})$ are the flux vectors along x and y, respectively; $\mathbf{H}_x(\mathbf{U})$ and $\mathbf{H}_y(\mathbf{U})$ are vectors representing the forces exchanged between the flow and the obstacles along the x- and y-directions; $\mathbf{B}_x(\mathbf{U})$ and $\mathbf{B}_y(\mathbf{U})$ are vectors representing the forces exchanged between the flow and the non-horizontal bed along x and y; $\mathbf{S}_f(\mathbf{U})$ is a flow resistance vector, where the components $S_{f,x}$ and $S_{f,y}$ take into account not only the bed friction but also additional forces arising from space-averaging of SWE point variables (Velickovic 2012). The terms $\mathbf{H}_x(\mathbf{U})\partial\varphi/\partial x$, $\mathbf{H}_y(\mathbf{U})\partial\varphi/\partial y$, $\varphi\mathbf{B}_x(\mathbf{U})\partial z/\partial x$, and $\varphi\mathbf{B}_y(\mathbf{U})\partial z/\partial y$, are called non-conservative products because they cannot be written in divergence (i.e., conservative) form, requiring careful mathematical and numerical treatment when geometric discontinuities are present (Dal Maso et al. 1995, Muñoz-Ruiz and Parés 2007, Castro et al. 2008, Cozzolino et al. 2018).

The left-hand side of Eq. (1) exhibits properties such as hyperbolicity and invariance to translation and rotation, while the celerity of moving small disturbances is equal to that exhibited by the classic SWE model (Guinot and Soares-Frazão 2006, Castro et al. 2007, Ferrari et al. 2017). Notice that the storage porosity φ in Eq. (1) is isotropic because it is a scalar quantity depending on the position only but not on the direction. Unresolved anisotropic effects (shape drag, mechanical dispersion, formation of preferential flow paths) can be taken into account by means of the anisotropic flow resistance vector $\mathbf{S}_f(\mathbf{U})$ (Velickovic et al. 2017, Viero and Valipour 2017, Viero 2019, Ferrari et al. 2019, Ferrari and Viero 2020).

To cope with the limitations of the SP model, the differential Binary Single Porosity (BSP) model by Varra et al. (2020) was introduced to allow for a local definition of the urban fabric geometric characteristics. In the present paper, the BSP model is enhanced by considering the effects of friction and variable bed elevation. The corresponding mathematical derivation (see Appendix A for details) supplies:

$$(3)\quad \frac{\partial I\mathbf{U}}{\partial t}+\frac{\partial I\mathbf{F}(\mathbf{U})}{\partial x}+\frac{\partial I\mathbf{G}(\mathbf{U})}{\partial y}+\mathbf{H}_x(\mathbf{U})\frac{\partial I}{\partial x}+\mathbf{H}_y(\mathbf{U})\frac{\partial I}{\partial y}+I\mathbf{B}_x(\mathbf{U})\frac{\partial z}{\partial x}+I\mathbf{B}_y(\mathbf{U})\frac{\partial z}{\partial y}=I\mathbf{S}_f(\mathbf{U}).$$

In Eq. (3), $I(x,y)$ is an isotropic binary indicator function (Fig. 1a) such that $I(x,y) = 0$ if the point (x,y) falls on a building while $I(x,y) = 1$ if the point (x,y) falls into a void among buildings, which are assumed to be perfectly rigid and impenetrable to the flood flow. The distribution of $I(x,y)$ can be easily evaluated from digital terrain models or airborne imagery (Sanders et al. 2008).

The comparison between Eqs. (1) and (3) shows that the left-hand side of Eq. (3) formally coincides with the left-hand side of Eq. (1) where the symbol $I(x,y)$ substitutes the symbol $\varphi(x,y)$. This implies that the BSP model of Eq. (3) inherits all the relevant mathematical properties (hyperbolicity, rotation and translation invariance, celerity of small disturbances) of the left-hand side of Eq. (1). However, the BSP model avoids space averaging of the SWE model in an REA because it directly incorporates the buildings through the binary indicator function $I(x,y)$, as shown in Appendix A, implying that all the variables in Eq. (3) must be intended as local values. For this reason, the components $S_{f,x}$ and $S_{f,y}$ of $\mathbf{S}_f(\mathbf{U})$ in Eq. (3) represent the local bed shear stress and can be evaluated employing classic friction models such as Manning's formulas $S_{f,x}=n_M^2 u\sqrt{u^2+v^2}/h^{4/3}$ and $S_{f,y}=n_M^2 v\sqrt{u^2+v^2}/h^{4/3}$, where n_M is the roughness coefficient.

Remark 1. By construction, the BSP model coincides with the SWE model in the voids among the buildings. We observe from Eq. (3) that the position $I(x,y) = 1$ exactly supplies the SWE model after the obvious simplifications. For more details about this consistency property, the reader is addressed to Appendix A.

[Insert Figure 1 about here]

2.2 Finite Volume numerical model

In the present work, the solution of the 2-d BSP model [Eq. (3)] is tackled employing a first-order FV scheme on unstructured triangular grids (Figs. 1b,c), where the following computational variables

$$\varphi_i = \frac{1}{|\Omega_i|}\int_{\Omega_i} I(x,y)\,d\Omega, \quad z_i = \frac{1}{\varphi_i|\Omega_i|}\int_{\Omega_i} I(x,y)\,z(x,y)\,d\Omega,$$
$$\mathbf{U}_i^n = \frac{1}{\varphi_i|\Omega_i|}\int_{\Omega_i} I(x,y)\,\mathbf{U}(x,y,t^n)\,d\Omega, \tag{4}$$

are the numerical approximations of the relevant flow and geometric variables in the i-th control volume Ω_i. In Eq. (4), the meaning of the symbols is as follows: $|\Omega_i|$ is the area of the computational cell Ω_i; z_i is the cell-averaged value of the bed elevation $z(x,y)$; the cell-averaged value $\varphi_i \in [0, 1]$ of the binary indicator function $I(x,y)$ is the fraction of computational cell area in Ω_i that is occupied by voids; finally, $\mathbf{U}_i^n = \left(h_i^n \quad h_i^n u_i^n \quad h_i^n v_i^n\right)^T$ is the vector of the SWE cell-averaged conserved variables at the n-th time level $t^n = n\Delta t$, where Δt is the numerical time step. The cells of the domain discretization may overlap the buildings (Fig. 1b), and their sides are not constrained to follow the buildings perimeters. For this reason, the presence of blocking elements in the cell is accounted for by $\varphi_i < 1$, based on the superposition of the computational cell with the footprint of the obstacles (Fig. 1c).

According to the BSP model of Eq. (3), the evolution of $\mathbf{U}_i^n$ is driven in each cell by appropriate numerical approximations of fluxes, non-conservative products, and friction terms. However, the Finite Volume cell-averaging process of Eq. (4) causes the formation of flow and geometric variables discontinuities at cell interfaces (Fig. 1c), implying that fluxes and non-conservative products appearing in Eq. (3) are conveniently computed by approximating the solution of a local plane Riemann problem (Godlewski and Raviart 1996).

To clarify the nature of such a Riemann problem, we observe that the BSP model is formally the restriction of the SP model to the case $\varphi(x, y) = I(x, y)$. It follows that we must solve an SP Riemann problem at the interface E_{ij} between cells Ω_i and Ω_j, with left and right initial conditions defined by the cell-averaged approximations $\left(\mathbf{U}_i^n, \varphi_i, z_i\right)$ and $\left(\mathbf{U}_j^n, \varphi_j, z_j\right)$, respectively (see Fig. 1c). Despite the SP and BSP models coincide at the numerical level when the FV scheme is applied, the practical advantage of the BSP model over the original SP model is that the BSP porosity of Eq. (4) is defined at the numerical cell level, enabling to retain geometric details coarser than the cell itself.

With these premises, the FV scheme proposed in the present work (Eqs. [5] and [6] below) can be broken into four stages, as follows:

I. the cell-averaged conserved variables are preliminarily rotated to account for the local orientation of the cell interface;
II. the interface variables are reconstructed from the cell-averaged values;
III. numerical fluxes and non-conservative products are evaluated by approximating the solution of a cell interface SP Riemann problem;
IV. the cell-averaged conserved variables are advanced in time.

A time-splitting approach is adopted to separately treat the advective and the friction part of the mathematical model (Toro 2001). In the cell Ω_i, the vector $\mathbf{U}_i^n$ of the conserved variables at the time level n defined by Eq. (4) is first adjourned with the explicit advective step

$$(5)\quad \mathbf{U}_i^* = \mathbf{U}_i^n - \frac{\Delta t}{\varphi_i \left|\Omega_i\right|} \sum_{j \in N(i)} \left[\left|E_{ij}\right| \mathbf{R}_{ij}^{-1} \psi_{ij} \mathbf{\Phi}\left(\mathbf{V}_{ij}^-, \mathbf{V}_{ij}^+\right) - \mathbf{S}_{ij}^{z,-} - \mathbf{S}_{ij}^{\varphi,-} \right],$$

and then the fully implicit friction step (Varra et al. 2024)

$$\text{(6)}\ \mathbf{U}_i^{n+1} - \Delta t \mathbf{S}_f\left(\mathbf{U}_i^{n+1}\right) = \mathbf{U}_i^*$$

is subsequently used to calculate the vector $\mathbf{U}_i^{n+1}$ of the conserved variables at the time level $n + 1$.

In Eq. (5) and (6), the meaning of the symbols is as follows (compare with Fig. 1c): $\mathbf{U}_i^*$ is the vector of the conserved variables in the cell Ω_i after the advective step; $|\Omega_i|$ is the area of the cell Ω_i; $N(i)$ is the set of indices j such that Ω_j is a neighbour of Ω_i; $|E_{ij}|$ is the length of the edge E_{ij} between Ω_i and Ω_j, where $\mathbf{n}_{ij} = \left(n_{ij,x} \quad n_{ij,y}\right)^T$ is the normal to the interface E_{ij}, orientated from Ω_i to Ω_j, and such that $\mathbf{n}_{ij} = -\mathbf{n}_{ji}$; $\psi_{ij} \in \left[\min\left\{\varphi_i, \varphi_j\right\}, \max\left\{\varphi_i, \varphi_j\right\}\right]$ is a numerical approximation of the porosity at the interface E_{ij}, and it is computed based on the adjacent cell-averaged flow and porosity variables (see Varra et al. 2023 for additional details); $\mathbf{\Phi}\left(\mathbf{U}, \mathbf{V}\right)$ is the numerical flux vector corresponding to the plane SWE Riemann problem and such that $\mathbf{\Phi}\left(\mathbf{U}, \mathbf{U}\right) = \mathbf{F}\left(\mathbf{U}\right)$ (Godlewski and Raviart 1996); $\mathbf{R}_{ij}$ is a rotation matrix, defined as (Toro 2001)

$$\text{(7)}\ \mathbf{R}_{ij} = \begin{pmatrix} 1 & 0 & 0 \\ 0 & n_{ij,x} & n_{ij,y} \\ 0 & -n_{ij,y} & n_{ij,x} \end{pmatrix},$$

which allows the passage from the global reference framework Oxy to a local reference $Ox'y'$ whose x' and y' axes are aligned with the normal $\mathbf{n}_{ij} = \left(n_{ij,x} \quad n_{ij,y}\right)^T$ and the tangent $\mathbf{t}_{ij} = \left(-n_{ij,y} \quad n_{ij,x}\right)^T$ to the edge E_{ij}, respectively (Fig. 1c); finally, $\mathbf{S}_{ij}^{z,-}$ and $\mathbf{S}_{ij}^{\varphi,-}$ are the contributions to the cell Ω_i of the geometrical non-conservative product arising from bottom slope and porosity through the interface

E_{ij}, respectively. From Eq. (5), it is evident that the SP numerical flux is approximated by multiplying the SWE numerical flux $\mathbf{\Phi}$ by the numerical interface porosity ψ_{ij}. In the present algorithm implementation, $\mathbf{\Phi}$ is computed using a simplified version of the HLLC approximate Riemann solver (Toro 2001, Cozzolino et al. 2017).

A novel reconstruction procedure is proposed here (Appendix B) to compute the arguments $\mathbf{V}_{ij}^{-}$ and $\mathbf{V}_{ij}^{+}$ of the numerical flux $\mathbf{\Phi}$ and the interface porosity ψ_{ij}. The use of the reconstructed variables ψ_{ij}, $\mathbf{V}_{ij}^{-}$, and $\mathbf{V}_{ij}^{+}$, allows to cope with the alignment of the local reference *Ox*'*y*' and to satisfy special conditions like the well balancing on uneven beds in presence of variable porosity. In addition, it allows to introduce a specified local head loss at interface porosity jumps and to pick up the physically expected solution when the SP Riemann problem admits multiple exact solutions (Varra et al. 2021, 2023).

3. BSP model characterization

In the present section, the BSP model of Sec. 2 is characterised through a comparison with the results of a classic SWE model for a synthetic small-scale dam-break test case, and the consistency property (Remark 1) is verified.

3.1 Numerical experiment setup

A channel, which includes a reservoir surrounded by solid boundaries, a dam, and a floodplain with an idealized urban area, is 6.5 m long and 3.0 m wide (Fig. 2) and has a frictionless horizontal bed. The initial conditions are characterised by still water elevation h_0 = 0.4 m in the reservoir, which is separated from the downstream channel by a gate. The sudden opening of the gate generates a dam-break wave propagating in the floodplain, which is initially dry. Free-flow conditions are imposed along the entire floodplain perimeter.

[Insert Figure 2 about here]

The numerical BSP model (Sec. 2.2) is used to simulate the interaction between the dam-break wave and the buildings, and its results are compared with a reference solution supplied by a classic SWE model (Cozzolino et al. 2017). The 2-d domain is discretized using unstructured triangular meshes. Four computational meshes, named from ID1 to ID4, are generated using the software *Easymesh* by Bojan Niceno (Frey and Field 1991, Anderson 1994).

The uniform triangular mesh ID1, with average cell side $\Delta l = 0.01$ m, is obtained by excluding the buildings from the computational domain (*building hole method*, Schubert and Sanders 2012). This mesh exhibits more than twenty computational cells over the street width, satisfying the empirical requirement of ten computational cells for the accurate representation of complex 2-d wave patterns (Soares-Frazão and Zech 2008), and it is used for the SWE computations with resolved buildings by imposing solid-wall boundary conditions along the obstacle perimeter. The BSP simulations are run on three different uniform meshes (ID2, ID3, and ID4) covering the full domain, including the buildings. These grids, which are generated by using a *region-conforming* technique where the cell edges are aligned with the exterior boundary of the urban blocks (Sanders et al. 2008), have different grid sizes (Δl = 0.01, 0.05, and 0.2 m, respectively). The grid resolution of ID2 (Δl = 0.01 m) coincides with that of ID1, but the corresponding number of cells is greater because the mesh also encompasses the interiors of buildings. Finally, the grid resolution of ID3 ($\Delta l = 0.05$ m) is smaller than the geometrical length scale of the problem (the minimum streets' width is 0.20 m), while the resolution of ID4 is comparable with it.

The grid size and orientation influence the numerical representation of buildings in the BSP applications, where the obstacles are modelled through a discrete porosity field with $\varphi(x, y) = \varphi_i$ for $(x, y) \in \Omega_i$. Computational cells in very coarse meshes (with resolution comparable to or bigger than the geometrical urban scale) may overlap buildings or groups of buildings and streets, leading to a blurred representation of the obstacles. Conversely, when very refined grids are used, most of the computational cells entirely fall inside the buildings (where $\varphi_i = 0$) or in the voids among the buildings (where $\varphi_i = 1$), while only the cells overlapping the buildings perimeters exhibit $0 < \varphi_i < 1$. Fig. 3 represents the percentage of mesh area occupied by cells falling in one of the three porosity classes (i) $\varphi_i = 0$, (ii) $0 < \varphi_i < 1$, and (iii) $\varphi_i = 1$, showing that the domain area occupied by cells with porosity falling in the intermediate class (ii) $0 < \varphi_i < 1$ tends to zero with the mesh refinement. Thus, the mesh refinement produces the convergence of the discrete porosity field $\varphi(x,y)$ to the binary indicator function $I(x,y)$, enhancing the buildings' representation.

All the simulations are run using a 3.60 GHz Intel® Xeon® W-2123 CPU with 32 GB RAM The main characteristics of the simulations (model used, average cell side Δl, number N_{SWE} and N_{BSP} of cells in SWE and BSP computations, respectively) are reported in Table 1.

[Insert Table 1 about here]

[Insert Figure 3 about here]

3.2 Numerical results

Fig. 4 (left column) shows the spatial distribution of maximum water depths during the time interval $t \in [0.2, 20]$ s for the SWE and BSP simulations, while Fig. 4 (right column) shows the porosity fields corresponding to the grids used for the BSP simulations. Fig. 4a represents the reference SWE solution on fine grid with resolved buildings (ID1). Figs. 4b,c,d represent the BSP solutions on the grids ID2, ID3, and ID4, while Figs. 4e,f,g represent the corresponding porosity fields. In the panels with the porosity results, the trace of the building perimeters is superposed to the computational domain for better appreciating the effects introduced by the discrete porosity field.

The inspection of the reference SWE results (Fig. 4a, ID1) shows that the flow strongly interacts with the buildings during the simulation, causing the formation of bow wave shocks at the city entrance and of a water spillway at the exit, while a large dry area is formed in the wake of the north-east building and two minor dry areas are formed after the north-west and south-east buildings. The BSP porosity simulations (Figs. 4b,c,d) capture the main characteristics of the flow propagation, especially the bow shocks and the dry areas. In terms of maximum water depths, the main differences with the reference solution (ID1) can be found in a limited area located at the north-east corner of the domain, where the reference solution exhibits a dry bed, while the porosity applications present very small water depths (of the order of 10^{-3} m). However, the BSP results on the fine mesh ID2 ($\Delta l = 0.01$ m) do not coincide with the reference SWE results on the fine mesh ID1 ($\Delta l = 0.01$ m), due to the different treatment of obstacles and positioning of computational cells.

The BSP porosity results depend on the mesh resolution and tend towards the reference SWE solution for decreasing cell size, with two mechanisms acting on the BSP results quality. On one hand, finer grids reduce the numerical diffusion, as shown by the sharp profile of the bow shocks in Figs. 4b,c, while coarser grids tend to smoothen the flow details (Fig. 4d). On the other hand, finer grids improve the building representation, as evidenced by a comparison between the porosity fields of Figs. 4e,f,g.

Despite the assumption of impermeable buildings in Eq. (3), the BSP results on grid ID4 (Fig. 4d) exhibit extensive flow penetration in the areas occupied by buildings due to the blurred representation of their perimeter (Fig. 4g). We call this phenomenon *Benjamin's effect*, in honour of the German philosopher, W. Benjamin, who introduced the porosity concept to describe the interpenetration between buildings and social life in the city of Naples, Italy, during the early 20th century. The *Benjamin's effect* is a numerical artefact which has two competing consequences:

(i) a certain amount of water that is temporarily subtracted to further propagation through the urban fabric;

(ii) the loss of perfect imperviousness of the blocks allows the flow passage through them and the penetration in areas that could be potentially excluded from flooding in refined grid simulations.

However, Benjamin's effect is consistently reduced with grid refinement (meshes ID2 and ID3 of Figure 4b,c.

[Insert Figure 4 about here]

Fig. 5 depicts the spatial distribution of maximum flow velocities during the time interval $t \in [0.2, 20]$ s. In the reference SWE solution with resolved buildings (Fig. 5a) the maximum flow velocity is relatively high at the front side of the blocks and decreases passing through the inner area, while a strong central spillway is clearly visible at the city outlet. Expectedly, the BSP porosity simulations (Figs. 5b,c,d) experience a substantial reduction in flow propagation velocity, which is clearly accentuated by the grid coarsening. In particular, the BSP results with medium/coarse resolution (ID3 and ID4) do not satisfactorily capture the high flow velocity path along the main street and the spillway immediately downstream of the blocks. Other differences with the reference solution (ID1) can be found in the small area located at the northeast corner of the domain, where the reference solution is characterized by null velocity, while the porosity applications present higher values of the order of 1-2 m/s.

[Insert Figure 5 about here]

The maximum flow depths (h_{max}) and velocities (u_{max}) supplied by the SWE and BSP models during the simulations are sampled at N = 1096 points evenly distributed through the channel. In the following, the domain (excluding buildings and obstacles) is divided into three different zones (called A, B and C, as illustrated in Fig. 6): (i) Area C (in red) includes the streets among the buildings and represents the inner urban area; (ii) Area B (in blue) includes a limited strip immediately outside the building blocks and represents a transition region between the inner and the exterior parts of the built-up area; (iii) Area A (in green) encompasses the entire domain with the exclusion of Area B, Area C and the obstacles (in grey), thus representing the region outside the city.

In Figs. 7a,b,c, the h_{max} values for BSP simulations (y axis) on the progressively refined grids ID4, ID3, and ID2, respectively, are compared with the corresponding h_{max} values for the reference SWE simulation on the grid ID1 (x axis), considering the entire domain (A + B + C). Figs. 7a,b,c clearly show that the grid refinement makes the BSP flow depths converge to the reference SWE flow depths. To objectively assess the accuracy of the results, the Root Mean Square Error (RMSE) is computed using the definition

$$(8)\quad RMSE = \sqrt{\frac{1}{N}\sum_{i}^{N}\left(f^{i} - f_{ref}^{i}\right)^{2}}$$

where f^{i} is the solution of interest, f_{ref}^{i} is the reference solution, and i is the sample index. The inspection of Figs. 7a,b,c, where the RMSE(h_{max}) values are also reported, shows a decrease from RMSE = 0.015 m to RMSE = 0.002 m when passing from the mesh ID4 to ID2, confirming the reduction of the solution discrepancies between BSP and SWE flow depths for refining BSP grid. Interestingly, the inspection of Figs. 7a,b,c shows that the BSP h_{max} values approximate the SWE h_{max} values both from below and from above, implying that the flow depths supplied by the BSP are not generally higher (and then safer) than the SWE flow depths.

In Figs. 7d,e,f, a distinction is made between the h_{max}, supplied by the SWE and BSP simulations, evaluated at the points located in Area A (green dots), B (blue dots) and C (red dots), respectively. In Figs. 7d,e,f the corresponding RMSE values are also reported, showing a decrease from RMSE(A) = 0.013 m to RMSE(A) = 0.001 m, from RMSE(B) = 0.016 m to RMSE(B) = 0.002 m, and from RMSE(C) = 0.031 m to RMSE(C) = 0.008 m when passing from the mesh ID4 to ID2. This confirms the positive effect of the porosity grid reduction on the BSP solution accuracy both inside and outside the urban blocks. Interestingly, the lowest RMSE values are obtained in the Area A (outside the buildings area), the RMSE values in Area B (transition region) are very close to the ones of Area A, while the highest values characterise Area C (within the urban blocks), implying that the BSP solution in terms of flow depths is more accurate in the plain outside the built-up area.

In Figs. 8a,b,c, the maximum velocities u_{max} supplied by the SWE are compared with the corresponding values supplied by the BSP simulations. The inspection of the figures shows that, also in this case, the progressive refinement of the BSP grid leads to an error decrease. Interestingly, the u_{max} points (Figs. 8a,b,c) exhibit a greater dispersion around the panel bisectors when compared with the h_{max} (Figs. 7a,b,c). This suggests that, for a given grid size, the flow depth computation with the BSP porosity model is more reliable than the corresponding velocity computation. This is confirmed by the corresponding RMSE values, which slowly decrease from RMSE = 0.668 m/s to RMSE = 0.285 m/s when passing from the mesh ID4 to ID2 (Figs. 8a,b,c). Similar to the case of h_{max}, the BSP u_{max} velocities approximate the SWE u_{max} velocities both from below and from above. Of course, Figs. 8a,b,c exhibit a majority of dots below the quadrant bisector, implying that numerical dissipation effects have a role in reducing the BSP velocities with respect to the corresponding SWE velocities.

Figs. 8d,e,f represent the u_{max}, supplied by the SWE and BSP simulations, evaluated at the points located in Area A (green dots), B (blue dots) and C (red dots), respectively. The corresponding RMSE values exhibit a decrease from RMSE(A) = 0.584 m/s to RMSE(A) = 0.284 m/s, from RMSE(B) = 0.953 m/s to RMSE(B) = 0.278 m/s, and from RMSE(C) = 1.121 m/s to RMSE(C) = 0.311 m/s when passing from the mesh ID4 to ID2. This corroborates the influence of the porosity grid reduction on the BSP solution accuracy, both inside and outside the urban blocks. We note that the highest errors characterise Area C (inner urban area), implying that the BSP solution in terms of flow velocities is more accurate in the plain outside the built-up area. Finally, we observe in Fig. 8a a vertical line of dots where non-null BSP maximum velocities u_{max} correspond to null SWE u_{max}. This is because the BSP model predicts a wet domain with velocity different from zero in a small area located at the north-east corner of the domain (mainly included in Area A), where the reference

SWE solution is characterized by dry bed and rigorously null velocity (see Figs. 4 and 5). The RMSE values discussed above are also reported in Table 2.

In conclusion, the assessment of the BSP model for a small-scale dam-break case shows that, given a reference SWE solution on a fine grid with resolved buildings, the error between the BSP porosity results and the reference solution decreases with the porosity grid refinement, confirming the consistency condition stated in Remark 1. The same comparisons demonstrate that the BSP flow depth results rapidly tend to the reference SWE results, while the improvement of the BSP velocity results progresses more slowly, with a greater dispersion around the SWE results. This makes the flow depth evaluation with the BSP model inherently more robust than the corresponding velocity evaluation.

The inspection of Fig.7 shows that BSP flow depths approximate the corresponding SWE physical quantities both from above and below. Mass conservative numerical schemes, like the one used in the present numerical experiments, guarantee global conservation of the moving fluid volume, implying that the positive discrepancy between the BSP and SWE flow depths in some areas must be compensated by a corresponding negative discrepancy in other areas. It can be concluded that convergence of BSP Finite Volume results to the SWE solution can be never reached from a single direction (from below or above) in all the points of the computational domain. In other words, the BSP model does not systematically provide safer results (i.e., with higher flow depth) than the SWE model.

Finally, we observe that the BSP results, especially in terms of flow depth, are more satisfactory in the region outside the built-up area (Area A and B) for all porosity grid resolutions, while a consistent grid refinement is necessary to better capture the flow characteristics within the urban area (Area C). This result suggests that the BSP model could be used to complement the classic SWE model in a nesting cascade process where the BSP solution on a medium/coarse grid supplies the outer solution while the SWE model on a high-resolution grid is applied only where detailed calculations are required.

[Insert Figure 6 about here]

[Insert Figure 7 about here]

[Insert Figure 8 about here]

[Insert Table 2 about here]

4. BSP model validation

In the present Section, the 2-d BSP numerical model (Sec. 2.2) is validated by simulating the inundation process in a laboratory experiment (the Toce test case, Testa et al. 2007) and in a real-world dam-break event investing a complex urban area (the Tous dam-break, Alcrudo and Mulet 2007). Note that, even if the obstacles are not explicitly resolved in BSP computations, the footprint area of the buildings is represented (in grey) in all the following figures with numerical results. This facilitates the comparison with the reference SWE solutions, where the buildings are explicitly resolved. All the simulations are run using a 3.60 GHz Intel® Xeon® W-2123 CPU with 32 GB RAM.

4.1 Toce test case

The present benchmark - developed within the framework of the European IMPACT project and performed at CESI facilities in Milan (IMPACT 2004, Testa et al. 2007) - consists of an experimental flash flood across a simplified urban environment settled in the scale model of the Toce River Valley (Italy). The original experiments were conducted over two urban block layouts (aligned and staggered), two valley topographic distributions (original and modified), and by considering three inflow discharges (low, medium, and high). In the present work, the case with an aligned building layout settled in the original topographic configuration is considered (Fig. 9). This alignment evidences the presence of preferential paths from the West (upstream) to East (downstream) through the urban fabric. Eight gauges recording the water depth with time rate $\Delta t_r = 0.2$ s were located in the urban area, while two additional gauges were located at the inlet and in the reservoir of the experimental facility, respectively (Fig. 9).

In the simulations, the domain (initially dry) is flooded by imposing the low discharge hydrograph at the upstream boundary, while free outflow conditions are imposed at the downstream end. A uniform Manning roughness coefficient n_M = 0.0162 s m$^{-1/3}$ is assigned to the computational domain (Testa et al. 2007). In the reference SWE solution, the buildings are explicitly resolved on the uniform triangular fine grid ID1 with an average cell side of Δl = 0.01 m (Fig. 10a); the BSP model is run on two different grids, ID2 (Fig. 10b) and ID3 (Fig. 10c), with sides Δl = 0.05 and Δl = 0.15 m, respectively, which cover the full domain including the buildings. All grids are generated with *Easymesh*, using a *region-conforming* technique where the cell edges are aligned with the exterior boundary of the urban area (Sanders et al. 2008). The grid resolution of ID2 (Fig. 10b) is smaller than the geometrical length scale of the problem (the square blocks have a length side of 0.15 m, and the streets' width is 0.20 m), while the resolution of ID3 (Fig. 10c) is comparable with it. The main characteristics of the simulations (average cell side, numbers N_{SWE} and N_{BSP} of cells in SWE and BSP computations) are reported in Table 3.

[Insert Figure 9 about here]

[Insert Figure 10 about here]

[Insert Table 3 about here]

4.1.1 Spatial and temporal evolution of water depths and velocities

Fig. 11 represents the flow depths provided by the classic SWE model with resolved buildings on the fine grid ID1 and the corresponding BSP solutions on the coarse grids ID2 and ID3 for the times t = 20 s (left column) and t = 40 s (right column). The comparison between the SWE flow depth solutions at times t = 20 s and t = 40 s (Figs. 11a and 11b, respectively) and the corresponding BSP solutions on the grid ID2 (Figs. 11c and 11d) shows that the porosity simulations can reproduce the main features of the flow propagation. In particular, the high-flow depth region upstream of the urban layout and the downstream low-depth areas are satisfactorily reproduced. The comparison with the BSP solutions on the coarser grid ID3 (Figs. 11e and 11f) is obviously less accurate, due to the blurred modelling of obstacles and the increase of numerical diffusion.

A similar representation is provided in Fig. 12 for the flow velocities. The comparison between the reference SWE solutions with resolved buildings (Figs. 12a and 12b) and the corresponding BSP solutions on the ID2 grid (Figs. 12c and 12d) shows that the BSP model can delineate the low-velocity region immediately upstream of the urban layout and the preferential flow paths among the buildings, reproducing the spillways at the city exit. The grid coarsening (Figs. 12e and 12f, grid ID3) leads to a general attenuation of the velocity magnitude outside of the urban layout and to a poorer representation of the preferential flow paths between the blocks.

[Insert Figure 11 about here]

[Insert Figure 12 about here]

4.1.2 Time series of water depth

Figs. 13 and 14 compare the flow depth time series measured at the gauges of Fig. 9 (Testa et al. 2007) with those provided by the classic SWE model with resolved buildings (mesh ID1) and by the BSP model on the coarse grids ID2 and ID3. In general, SWE and BSP results show a good agreement with the measured values, with an obvious loss of accuracy due to grid coarsening in the BSP simulations.

The best agreement between numerical results (both SWE and BSP) and measured values is exhibited at gauges G3 and G4 (Fig. 13), located upstream of the urban layout, where the flow impact generates a backward moving shock with the formation of a subcritical flow area. Conversely, both the SWE and BSP simulations exhibit the greatest difference with the measured values at gauge G5 (Fig. 13), as already evidenced in previous works (Soares-Frazão et al. 2008, Sanders et al. 2008, Kim et al. 2014). This gauge is located on a preferential path immediately downstream of the first row of buildings, where the flow strongly accelerates after the impact on the obstacles. At gauge G10, located downstream of the urban layout, the BSP results underestimate the experimental data (Fig. 13), but the simulation with Δl = 0.05 m (upper panels) better agrees with the measured values than the simulation with Δl = 0.15 m (lower panels).

Gauges G6, G7, G8, and G9 are positioned around a building within the urban area (Fig. 9). For these locations, the porosity results with Δl = 0.05 m (Fig. 14, upper panels) are comparable with the resolved buildings ones and are in very good agreement with the experimental values; on the other hand, the porosity results with Δl = 0.15 m (Fig. 14, lower panels) always overestimate the experimental data, except at G8 where the simulations (with both resolved buildings and porosity approaches) tend to underestimate the measurements.

[Insert Figure 13 about here]

[Insert Figure 14 about here]

4.2 Tous dam-break test case

The Tous Dam failure case, which was selected as a benchmark under the European IMPACT project (IMPACT 2004), is detailed in Alcrudo and Mulet (2007) and only the information relevant for the setup of BSP and SWE models is reported here.

At about 19:15 on October 20, 1982, a significant part of the old Tous Dam in Spain, consisting of a zoned embankment with clay core and rockfill shells, failed and was swept away by the stream after an extreme rainfall event. The town of Sumacárcel, located downstream of the dam (Fig. 15), was severely affected, with flow depth reaching even 6-7 m in some places. The available dataset includes (but it is not limited to):

- a Digital Terrain Models (DTM) of the computational area realized in 1982, few weeks after the dam failure;

- an additional DTM, realized in 1998, after the construction of the new dam (Fig. 15a);
- the coordinates of the buildings situated in the town and some dispersed in the valley;
- the flood hydrograph evaluated during the post-event analysis;
- the recorded water levels in the Tous reservoir until the dam failure;
- the maximum water depth at 21 locations (illustrated in Fig. 15b).

The valley morphology in the 1982 DTM is strongly affected by the dam-break event, while the 1998 DTM exhibits a condition closer to that of the valley before the dam-break, thanks to remodelling by sediment transport. For this reason, only the results on the 1998 topography (Fig. 15a), which are in better agreement with the historical data, are shown in the present work.

[Insert Figure 15 about here]

SWE and BSP simulations are run on non-uniform triangular meshes with variable cell size over the computational domain: all the grids, obtained with *Gmsh* (Geuzaine and Remacle 2009), have a resolution of $\Delta l = 40$ m at the periphery of the computational domain, while a higher resolution is set over the urban area. Fig. 16a shows the refined mesh (ID1) produced for the reference SWE model with explicitly resolved buildings, providing a detailed view of the grid among the streets (Fig. 16b). In the urban area, the side of the ID1 mesh ($\Delta l = 2$ m) is the maximum compatible with the resolved buildings approach since it is comparable with the street widths. Two areas covered with orange trees that contributed to diverting the flood into the town during the dam-break are represented with green polygons in Fig. 16a. These orchard areas are modelled by means of a high value $n_{M2} = 0.075$ s m$^{-1/3}$ of the Manning's coefficient, while a uniform value $n_{M1} = 0.030$ s m$^{-1/3}$ is assumed in the remaining part of the domain (Alcrudo and Mulet 2007).

The BSP simulations are run on two different coarse meshes with resolution in the urban area of $\Delta l = 5$ (ID2) and $\Delta l = 10$ m (ID3), respectively. In Fig.16c, the mesh ID2 is represented for the entire valley, comprising the orchard areas, while a magnified view of the urban area is represented in Fig. 16d. Fig. 17 shows the porosity fields corresponding to the meshes ID2 and ID3 in the urban area. Clearly, the complex pattern of the urban area (with different-shaped buildings, narrow streets, and courtyards) is better reflected by the porosity distribution corresponding to mesh ID2 (Fig. 17a), whereas the mesh ID3 provides a poorer representation of the building perimeters, increasing the regions with partial blockage effects (orange, yellow and green values with permeability minor than one) and reducing the areas with total blockage effect (red values).

The main characteristics of the simulations (model type, cell sides in the urban area, numbers N_{SWE} and N_{BSP} of cells in SWE and BSP computations) are resumed in Table 4.

[Insert Table 4 about here]

[Insert Figure 16 about here]

[Insert Figure 17 about here]

In all the simulations, calculations are started with dry bed, whereas a free outflow is imposed at the downstream boundary condition. The available flood hydrograph from Tous Dam, lasting for a period of about two days, exhibits a peak discharge of 15000 m^3s^{-1} at 20:00 on October 20th. Conversely, maximum water depths were registered in the town of Sumacárcel at 19:40 on October 20th. Of course, the anticipation of the peak level in the town with respect to the peak discharge at the dam constitutes a physical discrepancy that must be corrected. For this reason, the flood hydrograph from Tous dam is first anticipated by half an hour (Fig. 18), and then applied as inflow boundary condition to the computational domain. Correspondingly, the water levels in the Tous reservoir reported in Alcrudo and Mulet (2007) are shifted by half an hour. Subsequently to the instant of dam failure by overtopping, water levels in the lake are evaluated considering the attainment of critical conditions across the breach.

[Insert Figure 18 about here]

4.2.1 Spatial evolution of water depths and velocities

With reference to the urban area, the numerical results obtained at 20:00 of October 20^{th} with the classic SWE model with resolved buildings (mesh ID1) are represented in Fig. 19a (water depths) and Fig. 20a (velocity field). A similar representation is made in Figs. 19b and 20b for the BSP simulation on the mesh ID2, and in Figs. 19c and 20c for the BSP simulation on the mesh ID3. The visual comparison suggests that the use of the porosity approach allows to capture the main characteristic of the flow propagation both outside and inside the city area. In particular, the BSP simulations can reproduce the drop of water heights from East to West in conjunction with the flow penetration in the city area (Fig. 19), with obvious loss of accuracy due to grid coarsening. However, the inundation extent provided by the porosity approach (Figs. 19b and 19c) is larger than the one simulated with the resolved buildings method (Fig. 19a). This is easily explained by recalling the *Benjamin's effect* introduced in Sec. 3.2: the building boundaries in BSP simulations lose their perfect imperviousness, and this allows the water to penetrate through them and reach further regions of the domain. Clearly, this phenomenon is more evident for the coarser grid ID3 (Fig. 19c), in accordance with the poorer representation of the building perimeters (Fig. 17b).

With reference to the flow velocities at 20:00 of October 20^{th}, the comparison between the reference SWE simulation (Fig. 20a) and the BSP simulations (Figs. 20b and 20c) shows that the porosity approach can capture the progressive flow deceleration from the high velocity area outside the city (red-orange values) to the low velocity area immediately to the east of the urban area and among the buildings (blue-violet values). Nonetheless, an interesting feature can be observed in the area immediately to the east of the urban settlement, namely the presence of a small recirculating pocket exhibited by the SWE results (Fig. 20a) whose diameter increases in the BSP simulations (Figs. 20b and 20c). The increase of the eddy diameter is evidently connected to the increase of numerical diffusion due to the coarsening of grids.

The total depth indicator (Aureli et al. 2008, Ferrari et al. 2019, Ferrari and Viero 2020)

(9) $D = h\sqrt{1+2Fr^2}$,

where h is the water height and Fr the Froude number, is a hazard index representing an equivalent measure of the total thrust exerted by the flow on the unit-width flow section. Fig. 21 presents the total depth indicator in the built-up area at 20:00 of October 20th for the SWE and BSP simulations using four hazard classes (lower-left panel in Fig. 21) defined as follows: low ($0 \le D < 0.5$ m), medium ($0.5 \le D < 1$ m), high ($1 \le D < 1.5$ m) and very high ($D \ge 1.5$ m). Fig. 21 shows that the difference between the SWE simulation on the mesh ID1 (Fig. 21a) and the BSP simulation on the mesh ID2 (Fig. 21b) is negligible for practical purposes. The increase of the cell size in the mesh ID3, characterized by a poorer representation of the building perimeter, extends the area where the class of very high total depth is evaluated (Fig. 21c).

[Insert Figure 19 about here]

[Insert Figure 20 about here]

[Insert Figure 21 about here]

4.2.2 Maximum water depths at historical locations

Fig. 22 compares the maximum water depth historical data at 21 locations (illustrated in Fig. 15b) with the results provided by the reference SWE model with resolved buildings on the mesh ID1 and by the BSP model on the coarse meshes ID2 and ID3. In some locations, different evaluations of the maximum flooding depth are available, and their range is represented (Alcrudo and Mulet 2007). The comparison shows that the simulated results exhibit a general good agreement with the recorded values and that the differences between the two approaches are moderate. Interestingly, there are three locations (gauges 15, 17, and 18) where both the SWE (grey bars) and the BSP (white and red bars) models supply flow depth greater than zero while the historically measured flow depth (black bars) is null. Moreover, there is a single location (gauge 9) where only the BSP model supplies flow depth greater than zero, and a single location (gauge 5) where only the historical measure and the BSP solution on the ID3 grid are greater than zero.

[Insert Figure 22 about here]

To objectively measure the discrepancies between the results of the resolved buildings and the porosity approaches, the root mean square error (RMSE) of maximum water depths at the available locations is evaluated and reported in Table 4. The reference SWE results on the mesh ID1 are superior to the results by the BSP model on the coarse meshes ID2 and ID3, due to the use of a finer grid with explicit representation of buildings. However, the use of the BSP model does not exceedingly magnify the results uncertainty.

4.3 Computational burden decrease

It is expected that the BSP model allows significant leverage of the computational time with respect to the SWE computations on fine grid, thanks to the use of coarser grids. This is confirmed by Table 5, where the fourth and fifth column contain the numbers N_{SWE} and N_{BSP} of computational cells corresponding to the meshes used for SWE and BSP computations, respectively, in the numerical experiments of Secs. 3 and 4. The sixth column of Table 5 reports, for each BSP mesh, the ratio $\sqrt{N_{SWE}/N_{BSP}}$, where N_{SBP} is the number of cells in the BSP mesh and N_{SWE} is the number of cells in the refined mesh used to obtain the reference SWE solution with resolved buildings. Finally, the last column of Table 5 reports, for each BSP mesh, the ratio T_{SWE}/T_{BSP} between the computational time T_{SWE} of the SWE reference solution on fine grid and the BSP computational time T_{BSP}.

The inspection of Table 5 shows that, for a given test, the increase of the ratio $\sqrt{N_{SWE}/N_{BSP}}$, which corresponds to a coarsening of the BSP mesh with respect to the refined SWE reference mesh, leads to an increase of the ratio T_{SWE}/T_{BSP}, i.e., to a decrease of the BSP computational burden with respect to the reference SWE computational burden. Except for the refined BSP mesh ID2 in the consistency test of Sec. 3 (second row of Table 5), $T_{SWE}/T_{BSP} > 1$ for all the numerical experiments, showing that the BSP model can be up to three orders of magnitude faster than the refined grid SWE model. This means that the BSP model allows a saving of computational resources with respect to the SWE computations when coarse grids are used. The exception of the very refined BSP mesh ID2 in the consistency test of Sec. 3 is easily explained recalling that this grid contains more cells than the reference SWE mesh ID1, because it covers the entire computational domain, buildings included, while the SWE exclude the obstacles from the mesh creation (building hole method).

A straightforward reasoning based on computational stability constraints shows that the computational time T_{SWE} in 2-d SWE numerical models decreases with the third power of the cell size Δl_{SWE} (Kim et al. 2014), i.e., $T_{SWE} \propto 1/\left(\Delta l_{SWE}\right)^3$. Since the number N_{SWE} of SWE computational cells approximately decreases with the second power of Δl_{SWE}, it follows that T_{SWE} scales with the third power of $\sqrt{N_{SWE}}$, i.e., $T_{SWE} \propto \left(\sqrt{N_{SWE}}\right)^3$. The representation of the values of T_{SWE}/T_{BSP} as a function of the corresponding $\sqrt{N_{SWE}/N_{BSP}}$ in Fig. 23 demonstrates that a similar concept is valid to estimate the speedup obtained with the BSP model. In fact, a simple nonlinear regression shows that this relationship can be nicely interpolated by the following power function

$$(10)\quad \frac{T_{SWE}}{T_{BSP}} = 1.06\left(\sqrt{\frac{N_{SWE}}{N_{BSP}}}\right)^{2.57}.$$

We observe that the computational speedup scales with the power 2.57 of the mesh ratio, which is close to the theoretic limit of 3. This theoretical limit cannot be reached because the computational complexity of the BSP numerical model is greater than that of the classic SWE model, due to the presence of the porosity non-conservative products.

[Insert Table 5 about here]

[Insert Figure 23 about here]

5. Conclusions

In the field of macroscopic modelling approaches for flood disaster prevention and mitigation in urban areas, the Binary Single Porosity (BSP) shallow water model has recently emerged as the theoretical connection between the classic Single Porosity (SP) shallow water model by Guinot and Soares-Frazão (2006) and the integral SWE model by Sanders et al. (2008). In the present paper, the original BSP model by Varra et al. (2020) has been generalized to the case of variable bed elevation with friction, and its approximate numerical solution has been tackled by means of a Finite Volume scheme where the cell-averaged value of the binary indicator function $I(x,y)$ represents the local storage porosity. In the adopted numerical approach, an SP Riemann solver supplies the numerical fluxes, while the hydrostatic reconstruction by Audusse et al. (2004) allows to approximate the effect of bed elevation jumps at the interfaces between two cells. Finally, the generalized hydrostatic reconstruction proposed by Varra et al. (2023) is used to approximate the effect of porosity jumps at the interfaces, picking the correct solution when multiple exact solutions are available, and introducing a dissipative mechanism at porosity discontinuities when the flow through a porosity reduction is supercritical.

The consistency test conducted in an idealized urban district shows that (i) the cell-averaged porosities converge to the binary indicator function $I(x,y)$, and (ii) the BSP results tend to the reference Shallow water Equations (SWE) solution for sufficiently refined grid, according to the consistency between the two models theoretically discussed in Section 2 and Appendix A. Two additional test cases, based on the Toce laboratory experiments (Testa et al. 2007) and the real-world Tous dam failure (Alcrudo and Mulet 2007), demonstrate the application of the BSP model to realistic conditions with complicate terrains and variable obstacle distributions. The comparison between the reference SWE solution on fine grid and the BSP solutions on coarse grids shows that the urban fabric representation by means of a discrete porosity field on coarse grids may lead to a partial loss of information about the urban geometry and to less accurate numerical results. However, the unavoidable loss of accuracy due to grid coarsening is compensated by the run time reduction achieved by the porosity simulations, which can vary depending to the case at hand. For the most complex case, the real-world Tous dam failure, a porosity simulation has proven to be nearly ten times faster than a SWE simulation on fine grid with explicitly resolved buildings.

Despite the accuracy loss, the reduction of computational cost makes the use of the BSP model promising in full-scale applications in urban environments when multiple simulations are needed to perform stochastic or scenario analysis, and no detailed information of local flow characteristics is required within the urban areas. A similar promising use of the BSP model is complementing the classic SWE model in a nesting cascade process where the SWE model on a high-resolution grid is applied only where necessary, while the BSP model supplies the outer solution with a coarser mesh. These lines of research will be pursued in the next future.

Author Declarations

The authors have no conflicts to disclose.

CRediT authorship contribution statement

Giada Varra: Conceptualization, Methodology, Visualization, Writing – original draft, Writing – review & editing, Software, Investigation, Formal Analysis. **Luca Cozzolino:** Conceptualization, Methodology, Writing – original draft, Writing – review & editing, Formal Analysis, Supervision.

Renata Della Morte: Writing – original draft, Writing – review & editing, Supervision. **Sandra Soares-Frazão:** Writing – original draft, Writing – review & editing, Supervision.

Acknowledgments

The work of Giada Varra is cofunded by the European Union program FSE-REACT-EU, PON Ricerca e Innovazione 2014-2020 DM1062/2021 (Grant No. CUP-I65F21001120001). Renata Della Morte and Luca Cozzolino would like to acknowledge the financial support from the project "Floods in cities: New insights for integrating pluvial flooding into flood risk management plans (INSPIRING)," funded by the Italian Ministry of University and Research (MUR) under the National Program PRIN2020 (Grant No. CUP-I65F21001820006).

The writers want to acknowledge the Editor and the Referees for their constructive comments that contributed to improving the manuscript's original version.

Appendix A. Derivation of the BSP model from the SWE model

The BSP model of Eq. (3) is improved with respect to the original BSP model by Varra et al. (2020) because the friction forces and the effects of variable bed elevation are included. In the present Appendix, we show how the BSP model of Eq. (3) can be derived from the classic 2-d SWE model (Dronkers 1964)

(A.1)
$$\begin{cases} \dfrac{\partial h}{\partial t}+\dfrac{\partial hu}{\partial x}+\dfrac{\partial hv}{\partial y}=0 \\ \dfrac{\partial hu}{\partial t}+\dfrac{\partial}{\partial x}\left(\dfrac{gh^2}{2}+hu^2\right)+\dfrac{\partial huv}{\partial y}+gh\dfrac{\partial z}{\partial x}=-ghS_{f,x} \\ \dfrac{\partial hv}{\partial t}+\dfrac{\partial huv}{\partial x}+\dfrac{\partial}{\partial y}\left(\dfrac{gh^2}{2}+hv^2\right)+gh\dfrac{\partial z}{\partial y}=-ghS_{f,y} \end{cases},$$

following the procedure described in Varra (2021).

The mathematical procedure for introducing the effect of impermeable obstacles into the SWE model of Eq. (A.1) consists of imposing that the velocity component orthogonal to the obstacle perimeter is null. This condition is represented by the additional equation

$$\text{(A.2)}\quad \mathbf{v}^T\mathbf{m} = 0,\ \mathbf{x} = \mathbf{x}_b,\ \mathbf{x}_b \in \partial\Omega_{v,b},$$

where $\mathbf{v} = \begin{pmatrix} u & v \end{pmatrix}^T$ is the velocity vector, $\mathbf{m} = \begin{pmatrix} m_x & m_y \end{pmatrix}^T$ is the normal unit vector (outward with respect to the fluid mass) along the obstacle perimeter $\partial\Omega_{v,b}$, $\mathbf{x} = (x, y)^T$ is the position vector in the plane (x, y), while $\mathbf{x}_b = (x_b, y_b)^T$ is the generic position along $\partial\Omega_{v,b}$.

The SWE model is valid among the obstacles, where the value of the binary function $I(x, y)$ is 1, but not inside obstacles, where $I(x, y) = 0$. The multiplication of Eq. (A.2) by $I(x, y)$ supplies

$$\text{(A.3)}\quad \begin{aligned}
&I\left(\frac{\partial h}{\partial t} + \frac{\partial hu}{\partial x} + \frac{\partial hv}{\partial y}\right) = 0,\\
&I\left[\frac{\partial hu}{\partial t} + \frac{\partial}{\partial x}\left(\frac{gh^2}{2} + hu^2\right) + \frac{\partial huv}{\partial y}\right] = -Igh\left(\frac{\partial z}{\partial x} + S_{f,x}\right),\\
&I\left[\frac{\partial hv}{\partial t} + \frac{\partial huv}{\partial x} + \frac{\partial}{\partial y}\left(\frac{gh^2}{2} + hv^2\right)\right] = -Igh\left(\frac{\partial z}{\partial y} + S_{f,y}\right),
\end{aligned}$$

which is meaningful among the buildings, where $I(x, y) = 1$, and it is identically null inside the obstacles, where $I(x, y) = 0$. Recalling that $\nabla I = -\mathbf{m}\delta\left(\mathbf{x} - \mathbf{x}_b\right)$, where $\delta\left(\mathbf{x} - \mathbf{x}_b\right)$ is the two-dimensional Dirac's delta centered in the points $\mathbf{x}_b$ (Defina 2000, Brocchini and Peregrine 2001), Eq. (A.3) can be rewritten as

$$
\begin{aligned}
&\frac{\partial Ih}{\partial t}+\frac{\partial Ihu}{\partial x}+\frac{\partial Ihv}{\partial y}=-h\mathbf{v}^T\mathbf{m}\delta\left(\mathbf{x}-\mathbf{x}_b\right),\\
&\frac{\partial Ihu}{\partial t}+\frac{\partial}{\partial x}\left(I\frac{gh^2}{2}+Ihu^2\right)+\frac{\partial Ihuv}{\partial y}-\frac{gh^2}{2}\frac{\partial I}{\partial x}=-hu\mathbf{v}^T\mathbf{m}\delta\left(\mathbf{x}-\mathbf{x}_b\right)-Igh\left(\frac{\partial z}{\partial x}+S_{f,x}\right),\\
&\frac{\partial Ihv}{\partial t}+\frac{\partial Ihuv}{\partial x}+\frac{\partial}{\partial y}\left(I\frac{gh^2}{2}+Ihv^2\right)-\frac{gh^2}{2}\frac{\partial I}{\partial y}=-hv\mathbf{v}^T\mathbf{m}\delta\left(\mathbf{x}-\mathbf{x}_b\right)-Igh\left(\frac{\partial z}{\partial y}+S_{f,y}\right).
\end{aligned}
\tag{A.4}
$$

The wall boundary condition prescribes $\mathbf{v}^T\mathbf{m}=0$ for $\mathbf{x}=\mathbf{x}_b$ while the condition $\delta\left(\mathbf{x}-\mathbf{x}_b\right)=0$ for $\mathbf{x}\neq\mathbf{x}_b$ is a property of the Dirac's delta function. This implies that the terms $\mathbf{v}^T\mathbf{m}\delta\left(\mathbf{x}-\mathbf{x}_b\right)$ at the right-hand side of Eq. (A.4) are identically null, supplying

$$
\begin{aligned}
&\frac{\partial Ih}{\partial t}+\frac{\partial Ihu}{\partial x}+\frac{\partial Ihv}{\partial y}=0,\\
&\frac{\partial Ihu}{\partial t}+\frac{\partial}{\partial x}\left(I\frac{gh^2}{2}+Ihu^2\right)+\frac{\partial Ihuv}{\partial y}-\frac{gh^2}{2}\frac{\partial I}{\partial x}=-Igh\left(\frac{\partial z}{\partial x}+S_{f,x}\right),\\
&\frac{\partial Ihv}{\partial t}+\frac{\partial Ihuv}{\partial x}+\frac{\partial}{\partial y}\left(I\frac{gh^2}{2}+Ihv^2\right)-\frac{gh^2}{2}\frac{\partial I}{\partial y}=-Igh\left(\frac{\partial z}{\partial y}+S_{f,y}\right),
\end{aligned}
\tag{A.5}
$$

which is nothing but the scalar form of Eq. (3).

From the construction, it is evident that the BSP model of Eq. (3) coincides with the SWE model of Eq. (A.1) where the obstacles have been directly incorporated into the model by means of Eq. (A.2). Since no averaging process is involved, the BSP model does not require the definition of a REA and the values of geometric and flow variables must be intended as point values.

Appendix B. Reconstruction of numerical variables

In the present Appendix, additional details are reported to describe the variables reconstruction used in the Finite Volume scheme of Sec. 2.2. In the following, we detail stages I and II, and the computation of non-conservative products during stage III.

Stage I: Rotation of the reference framework

The rotation of variables during stage I allows exploiting the rotation invariance property of the BSP model in the context of the SP plane Riemann problem solution. The conserved variables $\mathbf{U}_i^n$ and $\mathbf{U}_j^n$ in Ω_i and Ω_j are expressed in the rotated reference *Ox*'*y*' as

$$\text{(B.1)}\ \mathbf{V}_i = \begin{pmatrix} h_i & h_i\upsilon_i & h_i\tau_i \end{pmatrix}^T = \mathbf{R}_{ij}\mathbf{U}_i^n, \quad \mathbf{V}_j = \begin{pmatrix} h_j & h_j\upsilon_j & h_j\tau_j \end{pmatrix}^T = \mathbf{R}_{ij}\mathbf{U}_j^n$$

where the rotation matrix $\mathbf{R}_{ij}$ has been defined in Eq. (7). The rotation, which preserves the flow depth ($h_i = h_i^n$ and $h_j = h_j^n$), operates on the flow velocity components only. In Eq. (C.1), the Greek letters υ and τ are used to indicate the velocity components along *x*' and *y*', respectively.

Stage II: Interface variable reconstruction

The variables reconstruction of stage II aims to enforce special properties such as the well-balancing of steady solutions on uneven bed in presence of variable porosity (Greenberg and Leroux 1996, Audusse et al. 2004, Castro et al. 2007, Varra et al. 2023), the introduction of appropriate energy dissipation at geometric discontinuities (Varra et al. 2023, Eames and Robinson 2022), and the choice of the unique physically congruent solution when multiple alternatives are available (Varra et al. 2022, 2023).

To separately cope with the effects of porosity and bed elevation discontinuities, the variables reconstruction of stage II will be subdivided into a first step (*Step 1*), where the bed elevation jump is considered, and a second step (*Step 2*), where the porosity jump is involved. The Step 1 acts on the flow depth only, while the velocity components are unaffected. The Step 2 acts on flow depth and orthogonal component υ of the velocity, leaving the tangential velocity τ unaffected.

Step1. This step aims at enforcing the well-balancing property on uneven beds. First, a unique value $z_{ij} = \max\left(z_i, z_j\right)$ of the bed elevation is defined at the interface E_{ij}, then the variables

$$\text{(B.2)}\quad \begin{aligned} \mathbf{V}_{ij}^{HR,-} &= \left(h_{ij}^{HR,-} \quad h_{ij}^{HR,-}\upsilon_i \quad h_{ij}^{HR,-}\tau_i\right)^T \\ \mathbf{V}_{ij}^{HR,+} &= \left(h_{ij}^{HR,+} \quad h_{ij}^{HR,+}\upsilon_j \quad h_{ij}^{HR,+}\tau_j\right)^T \end{aligned},$$

are reconstructed from the rotated variables $\mathbf{V}_i$ and $\mathbf{V}_j$ by recomputing the flow depth with the algorithm by Audusse et al. (2004):

$$\text{(B.3)}\quad h_{ij}^{HR,-} = \max\left\{0, h_i + z_i - z_{ij}\right\}, \quad h_{ij}^{HR,+} = \max\left\{0, h_j + z_j - z_{ij}\right\}.$$

The conserved variables $\mathbf{V}_{ij}^{HR,-}$ and $\mathbf{V}_{ij}^{HR,+}$ are used during the algorithm stage III for the computation of the non-conservative products arising from the presence of the bed steps at the cell interfaces.

Step 2. Starting from the variables $\mathbf{V}_{ij}^{HR,-}$, $\mathbf{V}_{ij}^{HR,+}$, φ_i, and φ_j, the 1-d reconstruction approach by Varra et al. (2023) [see Sec. V A in Varra et al. (2023)] is used to evaluate the interface porosity ψ_{ij} through E_{ij} and reconstruct the variables

$$\text{(B.4)}\quad \begin{aligned} \mathbf{V}_{ij}^{\varphi,-} &= \left(h_{ij}^{\varphi,-} \quad h_{ij}^{\varphi,-}\upsilon_{ij}^{\varphi,-} \quad h_{ij}^{\varphi,-}\tau_i\right)^T, \quad \mathbf{V}_{ij}^{-} = \left(h_{ij}^{-} \quad h_{ij}^{-}\upsilon_{ij}^{-} \quad h_{ij}^{-}\tau_i\right)^T, \\ \mathbf{V}_{ij}^{\varphi,+} &= \left(h_{ij}^{\varphi,+} \quad h_{ij}^{\varphi,+}\upsilon_{ij}^{\varphi,+} \quad h_{ij}^{\varphi,+}\tau_j\right)^T, \quad \mathbf{V}_{ij}^{+} = \left(h_{ij}^{+} \quad h_{ij}^{+}\upsilon_{ij}^{+} \quad h_{ij}^{+}\tau_j\right)^T, \end{aligned}$$

leaving the tangential components of the velocity unaffected.

Contrary to existing reconstruction techniques (Audusse et al. 2004, Castro et al. 2007, Noelle et al. 2007) available in the literature, the reconstruction algorithm by Varra et al. (2023) produces two distinct reconstructed vectors $\mathbf{V}_{ij}^{\varphi,-}$ and $\mathbf{V}_{ij}^{-}$ to the left of the interface, and two other vectors $\mathbf{V}_{ij}^{\varphi,+}$ and $\mathbf{V}_{ij}^{+}$ on the right. This ingredient serves the purpose to pick-up the physically congruent solution among the alternatives when the exact SP Riemann problem admits more than one solution (Varra et al. 2020, Varra et al. 2021, Varra et al. 2022, Varra et al. 2023). While the vectors $\mathbf{V}_{ij}^{-}$ and $\mathbf{V}_{ij}^{+}$ are used for the computation of numerical flux and the porosity non-conservative product, the vectors $\mathbf{V}_{ij}^{\varphi,-}$ and $\mathbf{V}_{ij}^{\varphi,+}$ are used to compute the non-conservative product only.

Stage III: Numerical approximation of the non-conservative products

Once that the reconstructed variables are available from stage II, the numerical approximation of the non-conservative products are calculated. The contribution to the cell Ω_i of the geometrical non-conservative product arising from the bottom step through the interface E_{ij} is approximated by means of (Audusse and Bristeau 2005)

$$\text{(B.5)}\quad \mathbf{S}_{ij}^{z,-} = \varphi_i \left|E_{ij}\right| \begin{pmatrix} 0 \\ \dfrac{g}{2}\left[\left(h_i^n\right)^2 - \left(h_{ij}^{HR,-}\right)^2\right]\mathbf{n}_{ij} \end{pmatrix}.$$

Similarly, the contribution to the cell Ω_i of the geometrical non-conservative product arising from the porosity jump through the interface E_{ij} is approximated by means of (Cozzolino et al. 2018, Varra et al. 2023)

$$\text{(B.6)}\quad \mathbf{S}_{ij}^{\varphi,-} = \left|E_{ij}\right| \mathbf{R}_{ij}^{-1}\left[\psi_{ij}\mathbf{F}\left(\mathbf{V}_{ij}^{-}\right) - \varphi_i \mathbf{F}\left(\mathbf{V}_{ij}^{\varphi,-}\right)\right].$$

References

Alcrudo, F., & Mulet, J. (2007). Description of the Tous Dam break case study (Spain). Journal of Hydraulic Research, 45(Extra Issue), 45-57. Doi: 10.1080/00221686.2007.9521832.

Anderson W.K. (1994). A Grid Generation and Flow Solution Method for the Euler Equations on Unstructured grids. Journal of Computational Physics 110(1), 25-38. Doi: 10.1006/jcph.1994.1003.

Audusse E., Bouchut F., Bristeau M.-O., Klein R., Perthame B. (2004). A fast and stable well-balanced scheme with Hydrostatic Reconstruction for shallow water flows. SIAM Journal of Scientific Computing 25(6), 20150-2065. Doi: 10.1137/S1064827503431090.

Audusse E., Bristeau. M.O. (2005). A well-balanced positivity preserving second-order scheme for shallow water flows on unstructured meshes. Journal of Computational Physics 206(1), 311-333. https://doi.org/10.1016/j.jcp.2004.12.016

Benjamin W., Lacis A. (1925). *Neapel*. Frankfurter Zeitung, August 19th, 1925.

Bermúdez A., Vásquez M.E. (1994). Upwind methods for hyperbolic conservation laws with source terms. Computers & Fluids 23(8), 1049–107. Doi: 10.1016/0045-7930(94)90004-3.

Brocchini M., Peregrine D.H. (2001). The dynamics of strong turbulence at free surfaces. Part 2. Free-surface boundary conditions. Journal of Fluid Mechanics 449, 255-290. Doi: 10.1017/S0022112001006024.

Bruwier M., Archambeau P., Erpicum S., Pirotton M., Dewals B. (2017). Shallow-water models with anisotropic porosity and merging for flood modelling on Cartesian grids. Journal of Hydrology 554, 693-709. Doi: 10.1016/j.jhydrol.2017.09.051.

Bruwier M., Erpicum S., Archambeau P., Pirotton M., Dewals B. (2014). Mathematical formulation of shallow water models with porosity for urban flood modelling. In: Lehfeldt and Koppman Eds., ICHE 2014: Proceedings of the International Conference on Idroscience & Engineering, Hamburg, Germany, September 28 – October 2, 2014. Pages 159-166.

Castro M.J., LeFloch P.G., Muñoz-Ruiz v, Parés C. (2008). Why many theories of shock waves are necessary: convergence error in formally path-consistent scheme. Journal of Computational Physics, 227(17) 8107-8129. Doi: 10.1016/j.jcp.2008.05.012.

Castro M.J., Pardo Milanés A., Parés C. (2007). Well-balanced numerical schemes based on a generalized hydrostatic reconstruction technique. Mathematical Models and Methods in Applied Sciences 17(12), 2055-2113. Doi: 10.1142/S021820250700256X.

Cheema H.A., Rehan S.T., Shahid A., Head M.G., Jawad M.Y., Shah J. (2022). The mental health of children in flood-affected areas in Pakistan needs urgent attention. The Lancet Psychiatry 10(1), 7. Doi: 10.1016/S2215-0366(22)00381-9.

Costabile P., Macchione F. (2015). Enhancing river model set-up for 2-D dynamic flood modelling. Environmental Modelling & Software 67, 89-107. Doi: 10.1016/j.envsoft.2015.01.009.

Cozzolino, L., Pepe, V., Morlando, F., Cimorelli, L., D'Aniello, A., Della Morte, R., Pianese, D. (2017). Exact solution of the dam-break problem for constrictions and obstructions in constant width rectangular channels. ASCE J. Hydraul. Eng. 143 (11), 04017047.

Cozzolino L., Pepe V., Cimorelli L., D'Aniello A., Della Morte R., Pianese D. (2018). The solution of the dam-break problem in the Porous Shallow water Equations. Advances in Water Resources 114, 83-101. Doi: 10.1016/j.advwatres.2018.01.026.

Dal Maso G., LeFloch P.G., Murat F. (1995). Definition and weak stability of nonconservative products. Journal del Mathématiques Pures et Appliqués 74(6), 483-548.

Defina A. (2000). Two-dimensional shallow flow equations for partially dry areas. Water Resources Research 36(11), 3251-3264. Doi: 10.1029/2000WR900167.

Dewals B., Bruwier M., Pirotton M., Erpicum S., Archeambeau P. (2021). Porosity models for large-scale urban flood modelling: a review. Water 13(7), 960. Doi: 10.3390/w13070960.

Dronkers J.J. (1964) Tidal computations in rivers and coastal waters, North Holland, Amsterdam.

Eames I., Robinson T. (2022) Horizontal dam-break flow past a blocking-drag region, Physics of Fluids 34, 052104. Doi: 10.1063/5.0079188.

Ferrari A., Vacondio R., Dazzi S., Mignosa P. (2017). A 1D-2D shallow water equations solver for discontinuous porosity field based on a generalized Riemann problem. Advances in Water Resources 107, 233-249. Doi: 10.1016/j.advwatres.2017.06.023.

Ferrari A., Viero D.P., Vacondio R., Defina A., Mignosa P. (2019). Flood inundation modeling in urbanized areas: A mesh-independent porosity approach with anisotropic friction. Advances in Water Resources 125, 98-113. Doi: 10.1016/j.advwatres.2019.01.010.

Ferrari A., Viero D.P. (2020). Floodwater pathways in urban areas: a method to compute porosity fields for anisotropic subgrid models in differential form. Journal of Hydrology 589, 125193. Doi: 10.1016/j.jhydrol.2020.125193.

Finaud-Guyot, P., Delenne, C., Lhomme, J., Guinot, V., & Llovel, C. (2010). An approximate-state Riemann solver for the two-dimensional shallow water equations with porosity. Int. J. Numer. Meth. Fluids, 62, 1299-1331.

Frey W.H., Field D.A. (1991). Mesh Relaxation: A New Technique for Improving Triangulations. International Journal for Numerical Methods in Engineering 31(6), 1121-1133. Doi: 10.1002/nme.1620310607.

Gel'fand J.M., Shilov G.E. (1964). Generalised functions. Vol. I, Properties and operations. Academic Press, New York.

Geuzaine C. and Remacle J. F. (2009). Gmsh: A 3-d finite element mesh generator with built-in pre- and post-processing facilities. International Journal for Numerical Methods in Engineering, 79(11), 1309-1331.

Godlewski E., Raviart P.-A. (1996). Numerical approximation of systems of hyperbolic equations. Springer, New York.

Gou L.-F., Zhu Z.-F., Liu S.-Y., Peng D.-Z., Zhang D.-W. (2024) Physical vulnerability of pedestrians under the joint effect of wind and floodwater and its application in urban block flooding:

Effects of urban block layout, building form and building array skyline, Physics of Fluids 36(4), 047116. Doi: 10.1063/5.0191951.

Greenberg J.M., Leroux A.Y. (1996). A well-balanec scheme for the numerical processing of source terms in hyperbolic equations. SIAM Journal of Numerical Analysis 33(1), 1-16. Doi: 10.1137/073300.

Guinot V. (2012) Multiple porosity shallow water models for macroscopic modelling of urban floods. Advances in Water Resources 37, 40-72. Doi: 10.1016/j.advwatres.2011.11.002.

Guinot V. (2017) Consistency and bicharacteristic analysis of integral porosity shallow water models. Explaining model oversensitivity to mesh design. Advances in Water Resources 107, 43-55. Doi: 10.1016/j.advwatres.2017.06.008.

Guinot V., Delenne C. (2014). Macroscopic modelling of urban floods. La Houille Blanche 6, 19-25. Doi: 10.1051/lhb/2014058.

Guinot V. Sanders B.F., Schubert J.E. (2017). Dual integral porosity shallow water model for urban flood modelling. Advances in Water Resources 103, 16-31. Doi: 10.1016/j.advwatres.2017.02.009.

Guinot V., Soares-Frazão S. (2006). Flux and source term discretization in two-dimensional shallow water models with porosity on unstructured grids. International Journal for Numerical Methods in Fluids 50(3), 309-345. Doi: 10.1002/fld.1059.

Horváth Z., Buttinger-Kreuzhuber A., Konev A., Cornel D., Komma J., Blöschl G., Noelle S., Waser J. (2019). Comparison of Fast Shallow-Water Schemes on Real-World Floods. Journal of Hydraulic Engineering 146(1). Doi: 10.1061/(ASCE)HY.1943-7900.000165.

IPCC, 2022: Climate Change 2022: Impacts, Adaptation, and Vulnerability. Contribution of Working Group II to the Sixth Assessment Report of the Intergovernmental Panel on Climate Change. Cambridge University Press, Cambridge. Doi:10.1017/9781009325844.

Jung J. (2022). Development of exact solution and finite volume method of porous shallow water equations for the analysis of urban flooding. PhD Thesis, Seoul National University, Seoul.

Kim B., Sanders B.F., Schubert J.E., Famiglietti J.S. (2014). Mesh type tradeoffs in 2D hydrodynamic modeling of flooding with a Godunov-based flow solver. Advances in Water Resources 68, 42-61. Doi: 10.1016/j.advwatres.2014.02.013.

Kim B., Sanders B.F., Famiglietti J.S., Guinot V. (2015). Urban flood modelling with porous shallow-water equations: A case study of model errors in the presence of anisotropic porosity. Journal of Hydrology 523, 680-692. Doi: 10.1016/j.jhydrol.2015.01.059.

Lhomme J. (2006). Modélisation des inondations en milieu urbain: approches unidimensionnelle, bidimensionnelle et macroscopique. PhD Thesis, Universite Montpellier II – Sciences e Techniques du Languedoc. (in French).

Mark O., Weesakul S., Apirumanekul C., Aroonnet S.B., Djordjević S. (2004). Potential and limitations of 1D modelling of urban flooding. Journal of Hydrology 299(3–4), 284-299. Doi: 10.1016/j.jhydrol.2004.08.014.

Muñoz-Ruiz M.L., Parés C. (2007). Godunov method for nonconservative hyperbolic systems. ESAIM: Mathematical Modelling and Numerical Analysis, 41(1) 169-185. Doi: 10.1051/m2an:2007011.

Nash S., Escauriaza C., Finaud-Guyot P., Wolfram J., Rousseau A. (2024) Single porosity model: Exploring the spatial resolution limits in complex urban patterns, Journal of Hydrology 131239. Doi: 10.1016/j.jhydrol.2024.131239.

Noelle S., Xing Y., Shu C.-W. (2007), High order well-balanced finite volume WENO schemes for shallow water equation with moving water, Journal of Computational Physics 226, 29-58. Doi: 10.1016/j.jcp.2007.03.031.

Özgen I., Zhao J.-h., Liang D.-f., Hinkelmann R. (2017). Wave propagation speeds and source term influences in single and integral porosity shallow water equations. Water Science and Engineering 10(4), 275-286. Doi: 10.1016/j.wse.2017.12.003.

Paterson D.L., Wright H., Harris P.A.H. (2018). Health risks of flood disasters. Clinical Infectious Diseases 67(9), 1450-1454. Doi: 10.1093/cid/ciy227.

Petaccia G., Soares-Frazão S., Savi F., Natale L., Zech Y. (2010) Simplified versus detailed two-dimensional approaches to transient flow modeling in urban areas. Journal of Hydraulic Engineering 136(4), 262-266. Doi: 10.1061/(ASCE)HY.1943-7900.0000154.

Sanders B.F., Schubert J.E., Gallegos H.A. (2008). Integral formulation of shallow-water equations with anisotropic porosity for urban flood modelling. Journal of Hydrology 362(1-2), 19-38. Doi: 10.1016/j.jhydrol.2008.08.009.

Sanders B.F., Schubert J.E. (2019) PRIMo: Parallel raster inundation model, Advances in Water Resources 126, 79-95. Doi: 10.1016/j.advwatres.2019.02.007.

Sanders B.F., Schubert J.E., Kahl D.T., Mach K.J., Brady D., Kouchak A.A., Forman F., Matthew R.A., Ulibarri N., Davis S.J. (2023). Large and inequitable flood risks in Los Angeles, California. Nature Sustainability 6, 47–57 (2023). Doi: 10.1038/s41893-022-00977-7

Schlegel L., Schulz V. (2022). Shape optimization for the mitigation of coastal erosion via porous shallow water equations. International Journal for Numerical Methods in Engineering 123(22), 5416-5441. Doi: 10.1002/nme.7074.

Schubert J.E., Sanders B.F. (2012). Building treatments for urban flood inundation models and implications for predictive skill and modelling efficiency. Advances in Water Resources 41, 49-64. Doi: 10.1016/j.advwatres.2012.02.012.

Soares-Frazão S., Zech Y. (2008). Dam-break flow through an idealised city. Journal of Hydraulic Research, 46(5), 45-64. Doi: 10.3826/jhr.2008.3164.

Soares-Frazão S., Lhomme J., Guinot V., Zech Y. (2008). Two-dimensional shallow-water model with porosity for urban flood modelling. Journal of Hydraulic Research, 46(1), 45-64. Doi: 10.1080/00221686.2008.9521842.

Soares-Frazão S., Franzini F., Linkens J., Snaps, J.-.C. (2018). Investigation of distributed-porosity fields for urban flood modelling using single-porosity models. In: Proceedings of the E3S Web of Conferences 40, 06040. Doi: 0.1051/e3sconf/20184006040 .

Testa, G., Zuccalà, D., Alcrudo, F., Mulet, J., & Soares-Frazão, S. (2007). Flash flood flow experiment in a simplified urban district. Journal of Hydraulic Research, 45(Extra Issue), 37-44. Doi: 10.1080/00221686.2007.9521831.

Toro E.F. (2001) Shock-capturing methods of free-surface flows, Wiley, Chichester.

Vacondio R., Dal Palù A., Ferrari A., Mignosa P., Aureli F., Dazzi S. (2017). A non-uniform efficient grid type for GPU-parallel Shallow Water Equations models. Environmental Modelling & Software 88, 119-137. Doi: 10.1016/j.envsoft.2016.11.012.

Varra G. (2021). Porous Shallow water Equations for urban flooding simulations. PhD Thesis, Parthenope University, Naples.

Varra G., Pepe V., Cimorelli L., Della Morte R., Cozzolino L. (2020). On integral and differential porosity models for urban flooding simulation. Advances in Water Resources 136, 103455. Doi: 10.1016/j.advwatres.2019.103455.

Varra G., Pepe V., Cimorelli L., Della Morte R., Cozzolino L. (2021) The exact solution to the Shallow water Equations Riemann problem at width jumps in rectangular channels, Advances in Water Resources 155, 103993. Doi: 10.1016/j.advwatres.2021.103993.

Varra G., Della Morte R., Gargano R., Cozzolino L. (2022). Porous Shallow-water Equations with the disambiguation of multiple solutions. Environmental Sciences Proocedings 21(1), 55. Doi: 10.3390/environsciproc2022021055.

Varra G., Della Morte R., Cimorelli L., Cozzolino L. (2023). Coping with geometric discontinuities in porous shallow water models. Physics of Fluids 35(10), 106612. Doi: 10.1063/5.0168385.

Varra G., Pepe V., Della Morte R., Cozzolino L. (2024). A novel efficient and robust treatment of the friction source term in 2D shallow water inundation models. Journal of Hydrology 634, 131045. Doi: 10.1016/j.jhydrol.2024.131045.

Velickovic M. (2012). Macroscopic modelling of urban flood by a porosity approach. Doctoral thesis, Université catholique de Louvain, Louvain.

Velickovic M., Zech Y., Soares-Frazão S. (2017). Steady-flow experiments in urban areas and anisotropic porosity model. IAHR Journal of Hydraulic Research 55(1), 85-100. Doi: 10.1080/00221686.2016.1238013.

Velickovic M., Van Emelen S., Zech Y., Soares-Frazão S. (2010). Shallow-water with porosity: sensitivity analysis to head losses and porosity distribution. In: Dittrich, Andreas; Koll, Katinka; Aberle, Jochen; Geisenhainer, Peter (Eds.): River Flow 2010. Karlsruhe: Bundesanstalt für Wasserbau. 613-620.

Viero D.P. (2019). Modelling urban floods using a finite element staggered scheme with an anisotropic dual porosity model. Journal of Hydrology 568, 247-259. Doi: 10.1016/j.jhydrol.2018.10.055.

Viero D.P., Valipour M. (2017). Modeling anisotropy in free-surface overland and shallow inundation flows. Advances in Water Resources 104, 1-14. Doi: 10.1016/j.advwatres.2017.03.007.

Whitaker S. (1969) Advances in the theory of fluid motion in porous media, Industrial & Engineering Chemistry 61(12), 14-28. Doi: 10.1021/ie50720a004.

Whitaker S. (1999) The method of volume averaging, Springer, Dordrecht.

Zhang J., Wu G., Liang B., Chen Y. (2023). Subgrid modeling of urban flooding incorporating buildings' effects. Physics of Fluids 35(12), 127108. Doi: 10.1063/5.0178816.

Tables List

Table 1. Consistency test. Main features of simulations.

Table 2. Consistency test. Resume of the RMSE values for maximum water depths and flow velocities on different grids.

Table 3. Toce River case. Main features of simulations.

Table 4. Tous dam-break event. Main features of simulations.

Table 5. Resume of mesh features and computational speedups.

Figures List

Figure 1. Distribution of the binary indicator function $I(x,y)$ in a generic domain with buildings (a). Finite Volume (FV) solution of the Binary Single Porosity (BSP) model: construction of the triangular grid overlapping the buildings (b); FV representation of the computational flow and geometric variables (c).

Figure 2. Consistency test. Plan view of the model geometry with distorted scale (a). Close-up of the buildings' layout (b). Measures in meters.

Figure 3. Consistency test. Relative distribution of porosity values within the cells for grids with progressively refined size: percentage of domain area occupied by cells with porosity falling in one of the three classes (i) $\varphi = 0$, (ii) $0 < \varphi < 1$, and (iii) $\varphi = 1$.

Figure 4. Consistency test. Maximum water depth for the reference solution with resolved buildings (a), and for the porosity simulations with $\Delta l = 0.01$ m (b), $\Delta l = 0.05$ m (c), and $\Delta l = 0.20$ m (d). Porosity fields for $\Delta l = 0.01$ m (e), $\Delta l = 0.05$ m (f), and $\Delta l = 0.20$ m (g).

Figure 5. Consistency test. Maximum flow velocity for the reference solution with resolved buildings (a), and for the porosity simulations with $\Delta l = 0.01$ m (b), $\Delta l = 0.05$ m (c), and $\Delta l = 0.20$ m (d).

Figure 6. Consistency test. Subdivision of the domain (excluding buildings and obstacles) in three different zones: Area C (red) including the streets among the buildings (inner urban area), Area

B (blue) surrounding the exterior of the building blocks (transition region), and Area A (green) encompassing the entire domain with the exclusion of Area B and C (outside the built-up area).

Figure 7. Consistency test. Comparison of maximum water depths under different grid sizes.

Figure 8. Consistency test. Comparison of maximum flow velocities under different grid sizes.

Figure 9. Topography of the Toce River Valley. Locations of buildings and monitoring stations.

Figure 10. Toce River case. Detail view of the meshes for the reference simulation with resolved buildings (a), and for porosity simulations with Δl = 0.05 m (b) and Δl = 0.15 m (c).

Figure 11. Toce River case. Top view of water depths at t = 20 s and t = 40 s, respectively, for the reference simulation with resolved buildings (a,b), and for the porosity simulations with Δl = 0.05 m (c,d) and Δl = 0.15 m (e,f).

Figure 12. Toce River case. Top view of velocity fields at t = 20 s and t = 40 s, respectively, for the reference simulation with resolved buildings (a,b), and for the porosity simulations with Δl = 0.05 m (c,d) and Δl = 0.15 m (e,f).

Figure 13. Toce River case. Water depth time series at gauges (3-5, 10): comparison between the experimental values (continuous black line) and the results of simulations with the classic SWE model with explicitly resolved buildings (white dots) and the porosity (BSP) model with Δl = 0.05 m and Δl = 0.15 m (grey dots).

Figure 14. Toce River case. Water depth time series at gauges (6-9): comparison between the experimental values (continuous black line) and the results of simulations with the classic SWE model with explicitly resolved buildings (white dots) and the porosity (BSP) model with Δl = 0.05 m and Δl = 0.15 m (grey dots).

Figure 15. Tous dam-break event. Digital model of the Júcar River reach from Tous Dam (top) to the city of Sumacárcel (bottom) after the construction of the new dam in 1998 (a). Locations of the gauges in the streets of Sumacárcel (b).

Figure 16. Tous dam-break event. Meshes on 1998 topography: a,b) refined mesh for the reference SWE model with explicitly resolved buildings; c,d) coarse mesh for the porosity (BSP) model with Δl = 5 m inside the city.

Figure 17. Tous dam-break event. Porosity fields for simulations with Δl = 5 m (a) and Δl = 10 m (a) in the urban area.

Figure 18. Tous Dam modified flood hydrograph, imposed as inflow boundary condition.

Figure 19. Tous dam-break event. Water depth (at 20:00 on October 20) for the reference simulation with resolved buildings (a), and for the porosity simulations with Δl = 5 m (b) and Δl = 10 m (c) in the city area.

Figure 20. Tous dam-break event. Velocity fields (at 20:00 on October 20) for the reference simulation with resolved buildings (a), and for the porosity simulations with Δl = 5 m (b) and Δl = 10 m (c) in the city area.

Figure 21. Tous dam-break event. Total depth (at 20:00 on October 20) for the reference simulation with resolved buildings (a), and for the porosity simulations with Δl = 5 m (b) and Δl = 10 m (c) in the city area.

Figure 22. Tous dam-break event. Maximum water depths at gauge locations: comparison between the measured values (in black) and the results obtained by the reference model with explicitly resolved buildings (in grey), and by the porosity (BSP) model with Δl = 5 m (in white) and Δl = 10 m (in red) within the built-up area.

Figure 23. Speedup versus mesh ratio: experimental points (dots) and regression curve (line).

Table 1. Consistency test. Main features of simulations.

Mesh ID	Model	Cell size Δl (m)	N_{SWE} (10^3)	N_{BSP} (10^3)
1	SWE	0.01	394.83	-
2	BSP	0.01	-	429.88
3	BSP	0.05	-	17.46
4	BSP	0.20	-	1.19

Table 2. Consistency test. Resume of the RMSE values for maximum water depths and flow velocities on different grids.

			RMSE(h_{max}) (m)				RMSE(u_{max}) (m/s)			
Mesh ID	Model	Cell size Δl (m)	Entire domain	Area A	Area B	Area C	Entire domain	Area A	Area B	Area C
1	SWE	0.01	-	-	-	-	-	-	-	-
2	BSP	0.01	0.002	0.001	0.002	0.008	0.285	0.284	0.278	0.311
3	BSP	0.05	0.010	0.008	0.008	0.026	0.543	0.498	0.634	0.900
4	BSP	0.20	0.015	0.013	0.016	0.031	0.668	0.584	0.953	1.121

Table 3. Toce River case. Main features of simulations.

Mesh ID	Model	Cell size Δl (m)	N_{SWE} (10^3)	N_{BSP} (10^3)
1	SWE	0.01	596.45	-
2	BSP	0.05	-	30.23
3	BSP	0.15	-	3.51

Table 4. Tous dam-break event. Main features of simulations.

Mesh ID	Model	Δl in the city (m)	N_{SWE} (10^3)	N_{BSP} (10^3)	RMSE(h) (m)
1	SWE	2	84.12	-	0.82
2	BSP	5	-	35.59	1.26
3	BSP	10	-	15.09	1.19

Table 5. Resume of mesh features and computational speedups.

Test	Mesh ID	Model	N_{SWE} (10^3)	N_{BSP} (10^3)	$\sqrt{N_{SWE}/N_{BSP}}$	T_{SWE}/T_{BSP}
Consistency test (Sec. 3)	1	SWE	394.83	-	-	-
	2	**BSP**	**-**	**429.88**	**0.895**	**0.8**
	3	BSP	-	17.46	4.76	89
	4	BSP	-	1.19	18.2	1708
Toce river (Sec. 4.1)	1	SWE	596.45	-	-	-
	2	BSP	-	30.23	4.44	52
	3	BSP	-	3.51	13.0	655
Tous dam-break (Sec. 4.2)	1	SWE	84.12	-	-	-
	2	BSP	-	35.59	1.54	2.4
	3	BSP	-	15.09	2.36	10.3

Figure 1. Distribution of the binary indicator function $I(x,y)$ in a generic domain with buildings (a). Finite Volume (FV) solution of the Binary Single Porosity (BSP) model: construction of the triangular grid overlapping the buildings (b); FV representation of the computational flow and geometric variables (c).

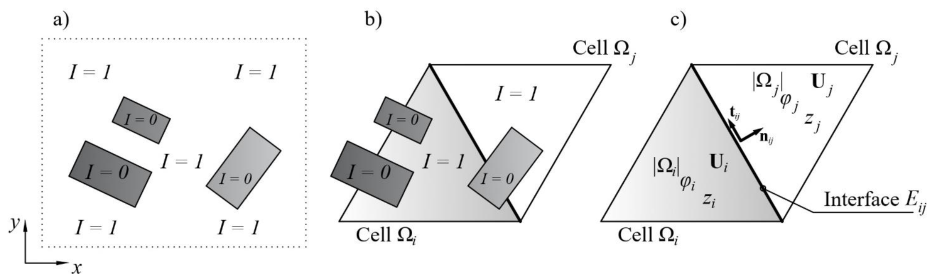

Figure 2. Consistency test. Plan view of the model geometry with distorted scale (a). Close-up of the buildings' layout (b). Measures in meters.

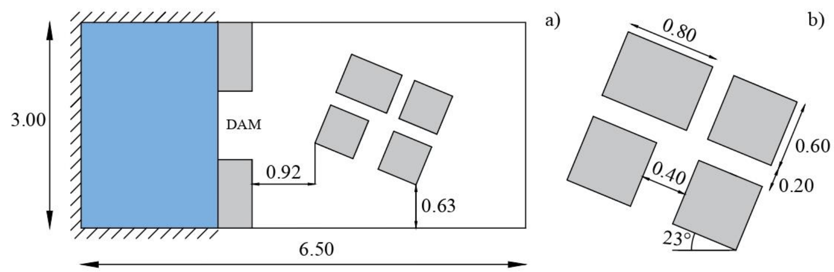

Figure 3. Consistency test. Relative distribution of porosity values within the cells for grids with progressively refined size: percentage of domain area occupied by cells with porosity falling in one of the three classes (i) $\varphi = 0$, (ii) $0 < \varphi < 1$, and (iii) $\varphi = 1$.

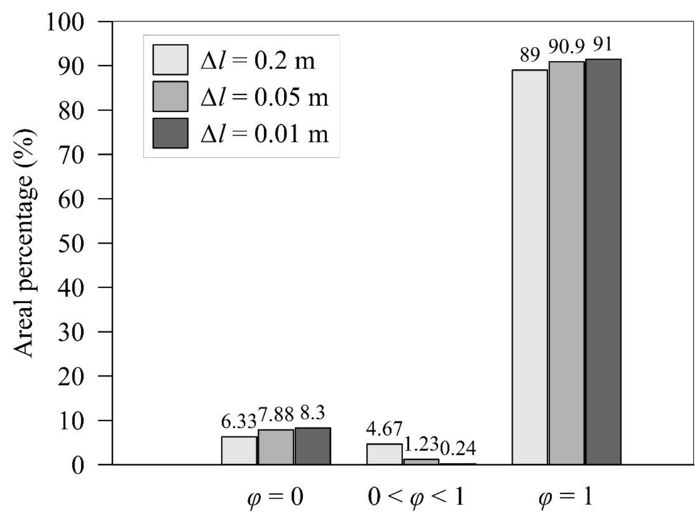

Figure 4. Consistency test. Maximum water depth for the reference solution with resolved buildings (a), and for the porosity simulations with Δl = 0.01 m (b), Δl = 0.05 m (c), and Δl = 0.20 m (d). Porosity fields for Δl = 0.01 m (e), Δl = 0.05 m (f), and Δl = 0.20 m (g).

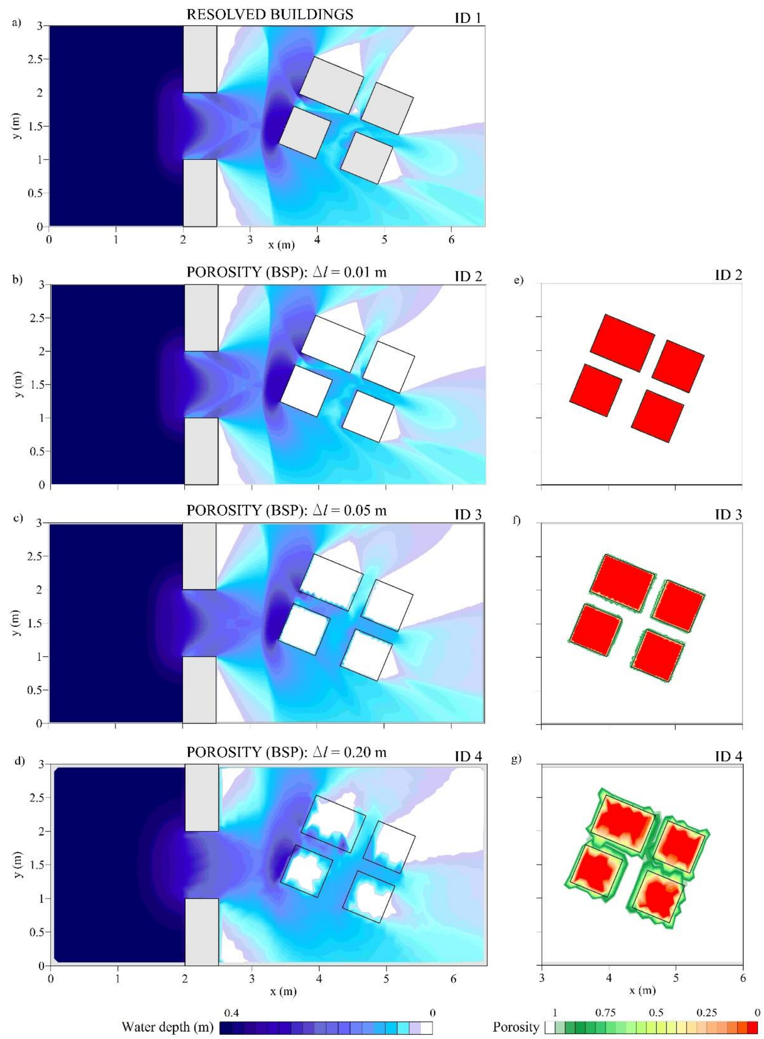

Figure 5. Consistency test. Maximum flow velocity for the reference solution with resolved buildings (a), and for the porosity simulations with Δl = 0.01 m (b), Δl = 0.05 m (c), and Δl = 0.20 m (d).

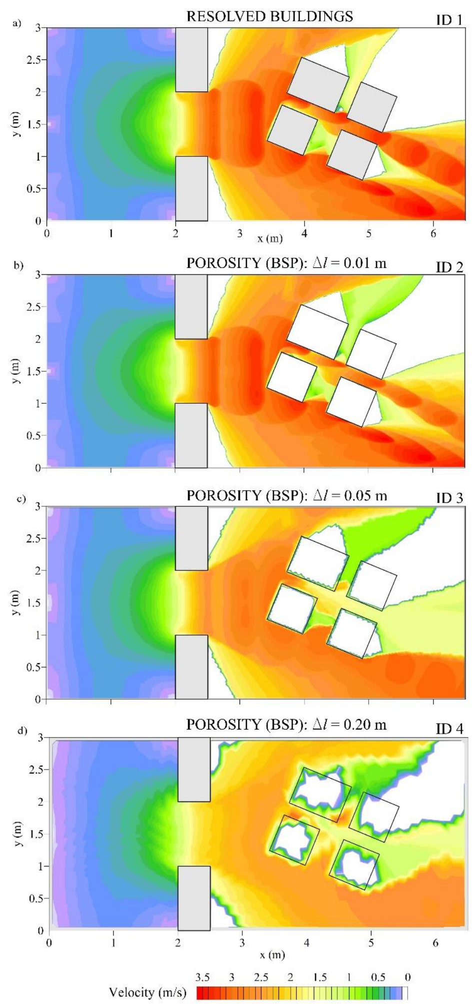

Figure 6. Consistency test. Subdivision of the domain (excluding buildings and obstacles) in three different zones: Area C (red) including the streets among the buildings (inner urban area), Area B (blue) surrounding the exterior of the building blocks (transition region), and Area A (green) encompassing the entire domain with the exclusion of Area B and C (outside the built-up area).

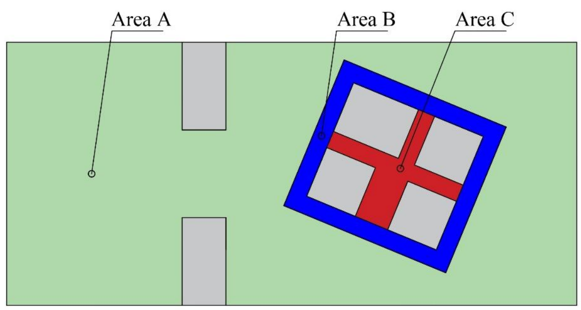

Figure 7. Consistency test. Comparison of maximum water depths under different grid sizes.

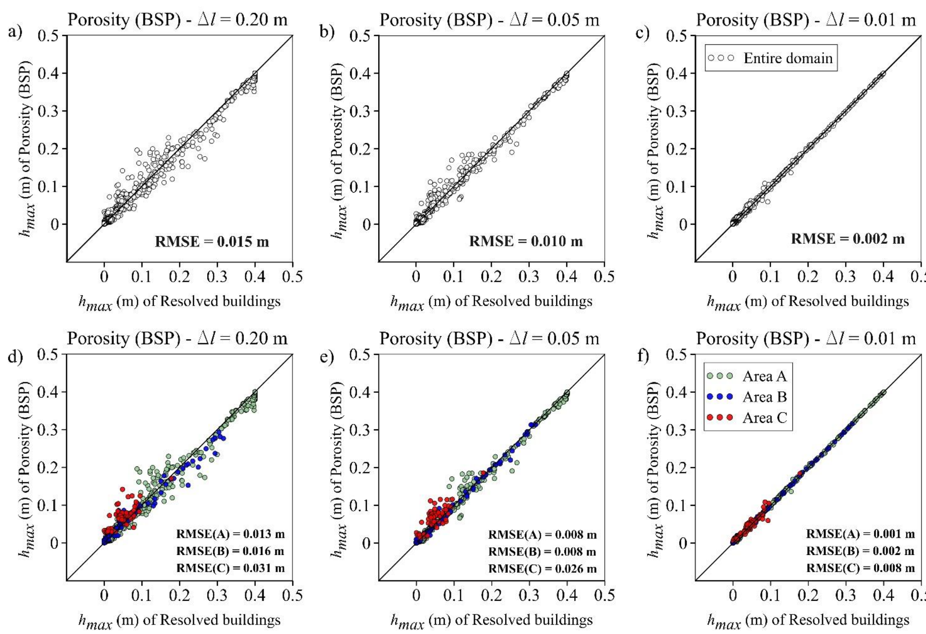

Figure 8. Consistency test. Comparison of maximum flow velocities under different grid sizes.

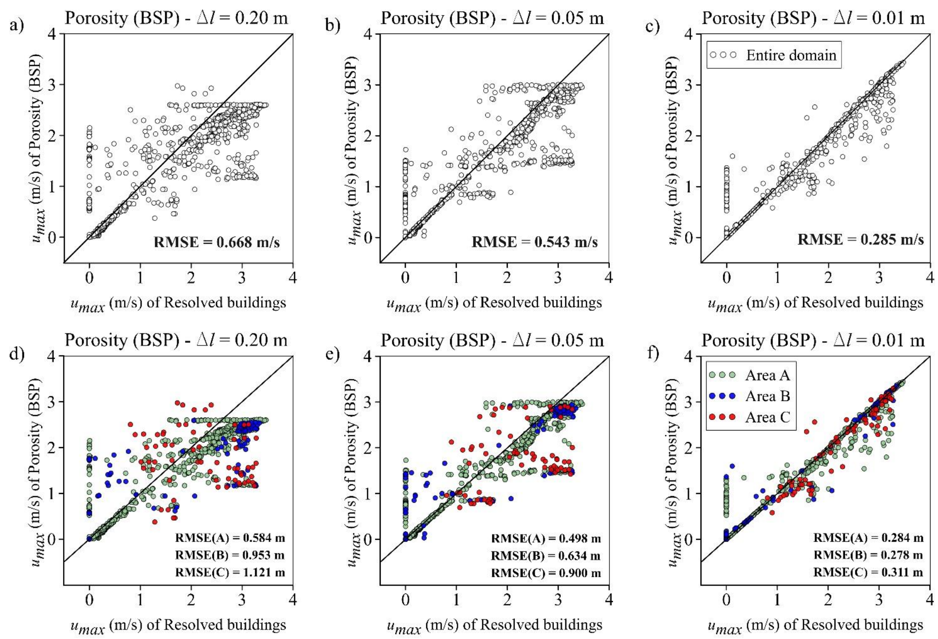

Figure 9. Topography of the Toce River Valley. Locations of buildings and monitoring stations.

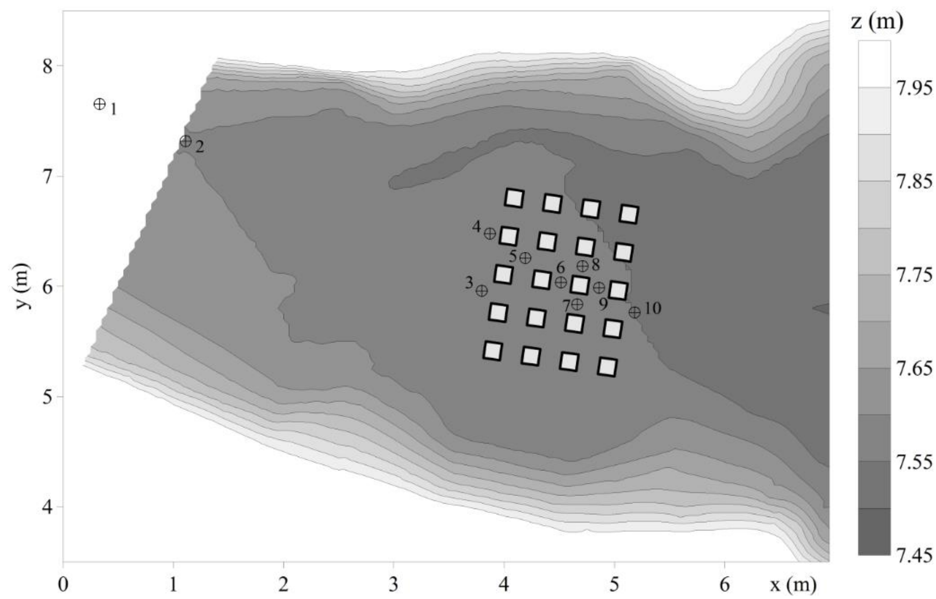

Figure 10. Toce River case. Detail view of the meshes for the reference simulation with resolved buildings (a), and for porosity simulations with Δl = 0.05 m (b) and Δl = 0.15 m (c).

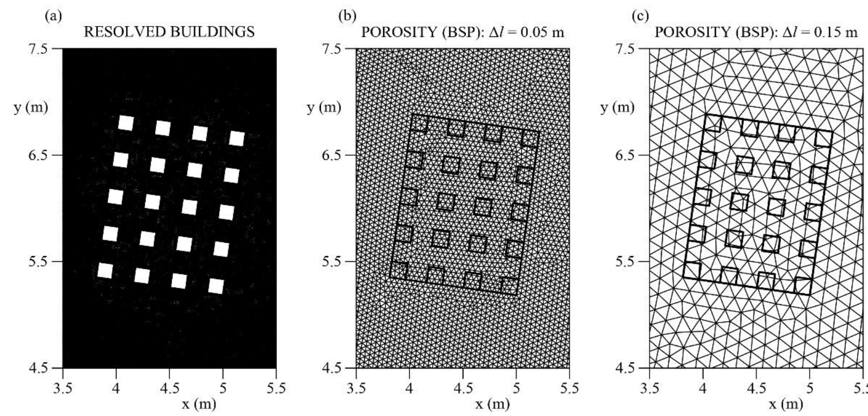

Figure 11. Toce River case. Top view of water depths at t = 20 s and t = 40 s, respectively, for the reference simulation with resolved buildings (a,b), and for the porosity simulations with Δl = 0.05 m (c,d) and Δl = 0.15 m (e,f).

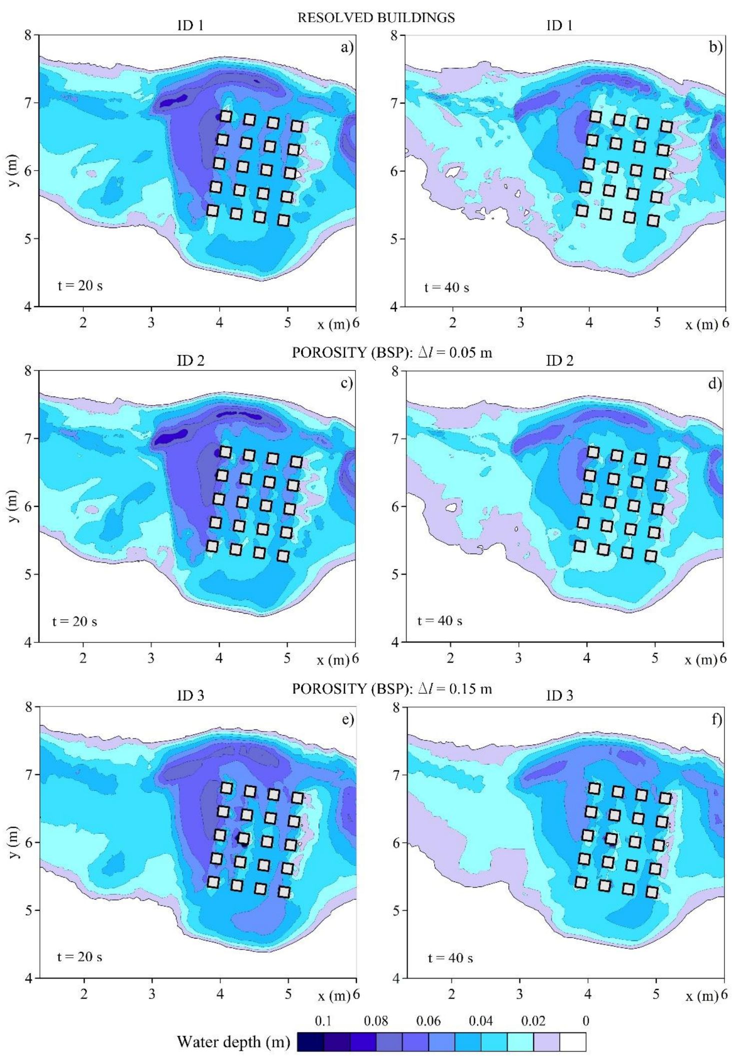

Figure 12. Toce River case. Top view of velocity fields at t = 20 s and t = 40 s, respectively, for the reference simulation with resolved buildings (a,b), and for the porosity simulations with Δl = 0.05 m (c,d) and Δl = 0.15 m (e,f).

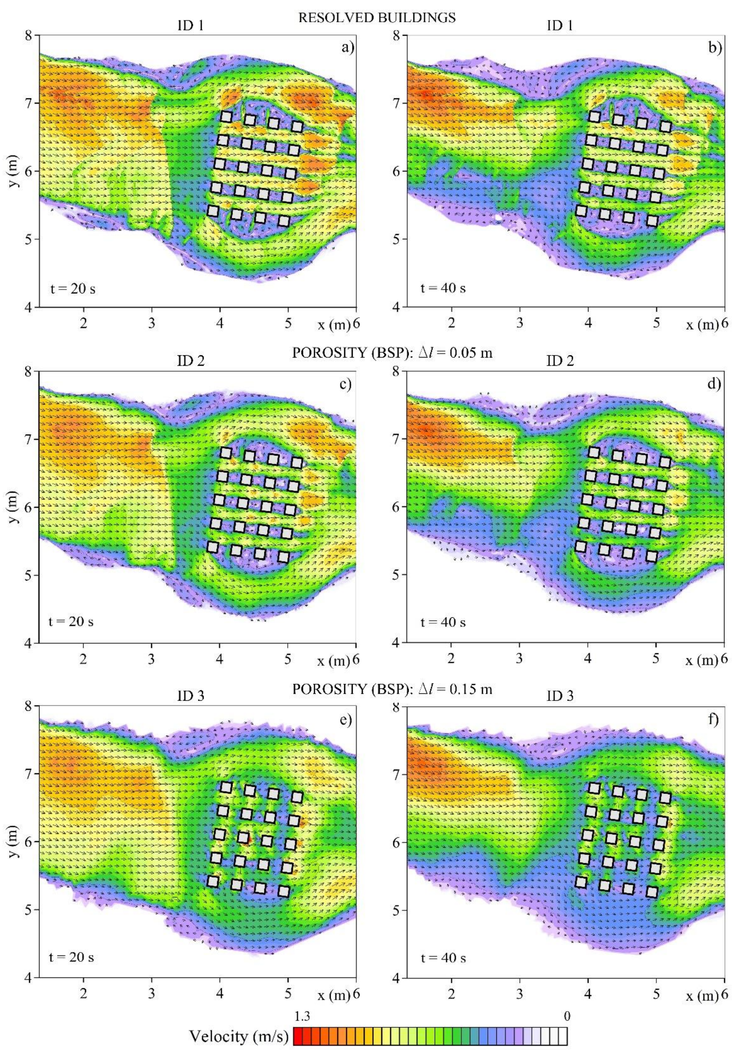

Figure 13. Toce River case. Water depth time series at gauges (3-5, 10): comparison between the experimental values (continuous black line) and the results of simulations with the classic SWE model with explicitly resolved buildings (white dots) and the porosity (BSP) model with Δl = 0.05 m and Δl = 0.15 m (grey dots).

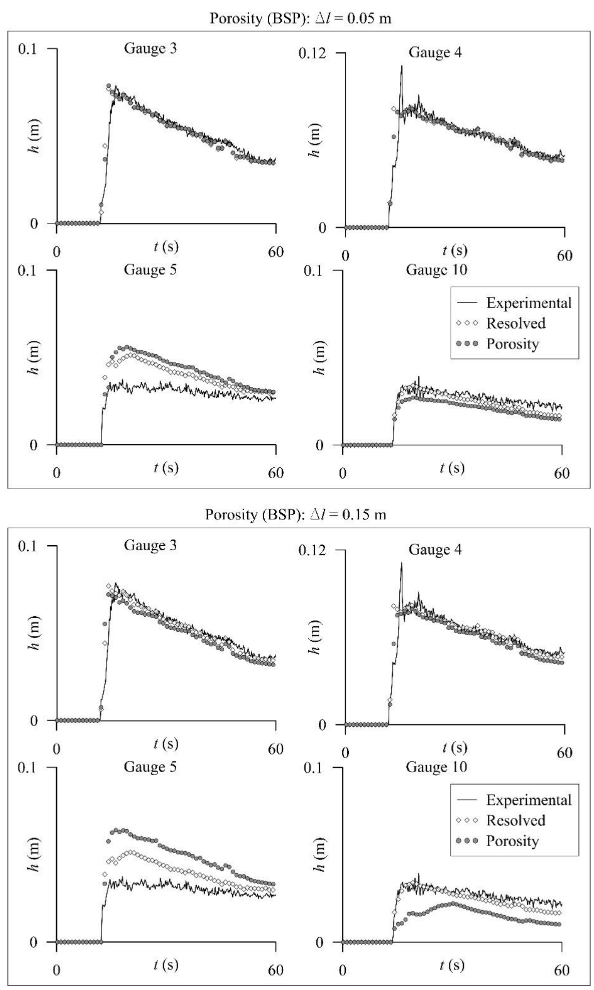

Figure 14. Toce River case. Water depth time series at gauges (6-9): comparison between the experimental values (continuous black line) and the results of simulations with the classic SWE model with explicitly resolved buildings (white dots) and the porosity (BSP) model with Δl = 0.05 m and Δl = 0.15 m (grey dots).

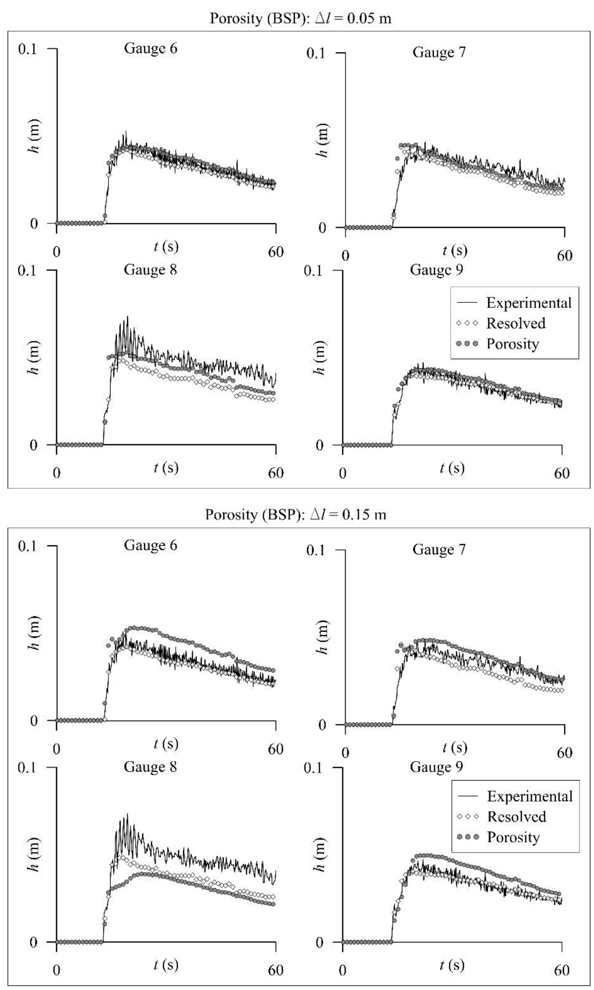

Figure 15. Tous dam-break event. Digital model of the Júcar River reach from Tous Dam (top) to the city of Sumacárcel (bottom) after the construction of the new dam in 1998 (a). Locations of the gauges in the streets of Sumacárcel (b).

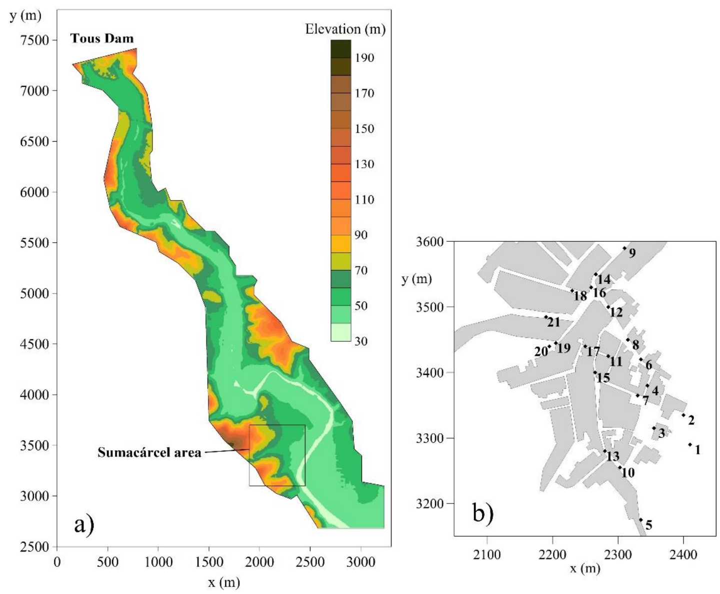

Figure 16. Tous dam-break event. Meshes on 1998 topography: a,b) refined mesh for the reference SWE model with explicitly resolved buildings; c,d) coarse mesh for the porosity (BSP) model with Δl = 5 m inside the city.

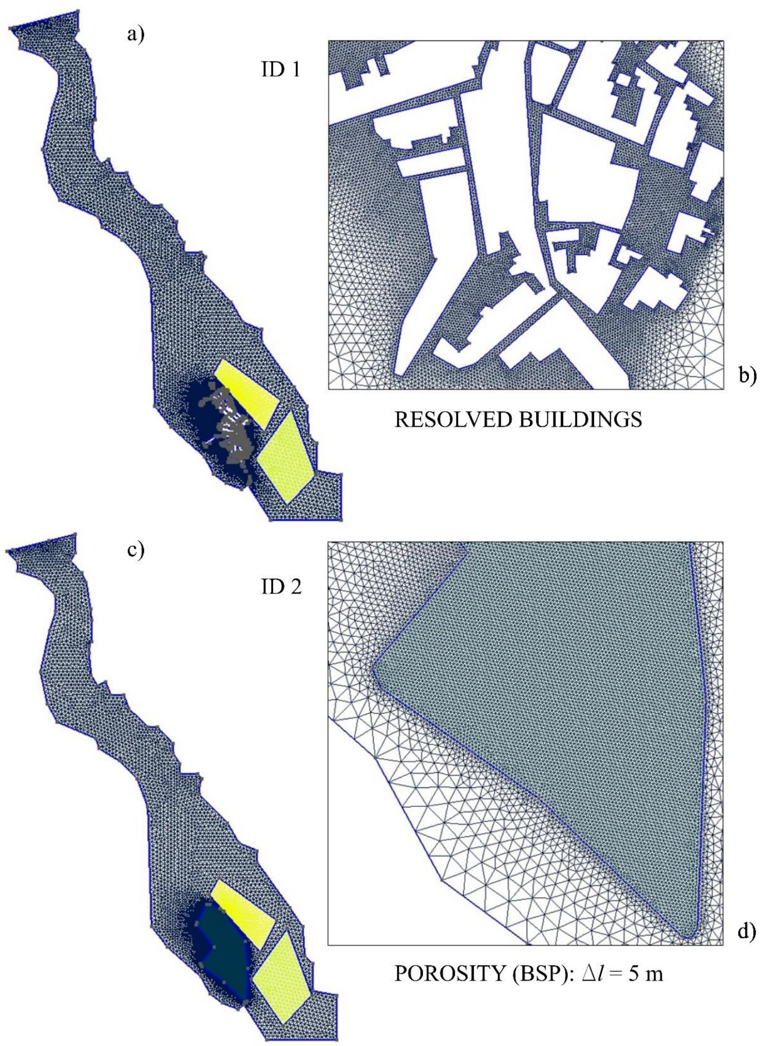

Figure 17. Tous dam-break event. Tous dam-break event. Porosity fields for simulations with $\Delta l = 5$ m (a) and $\Delta l = 10$ m (a) in the urban area.

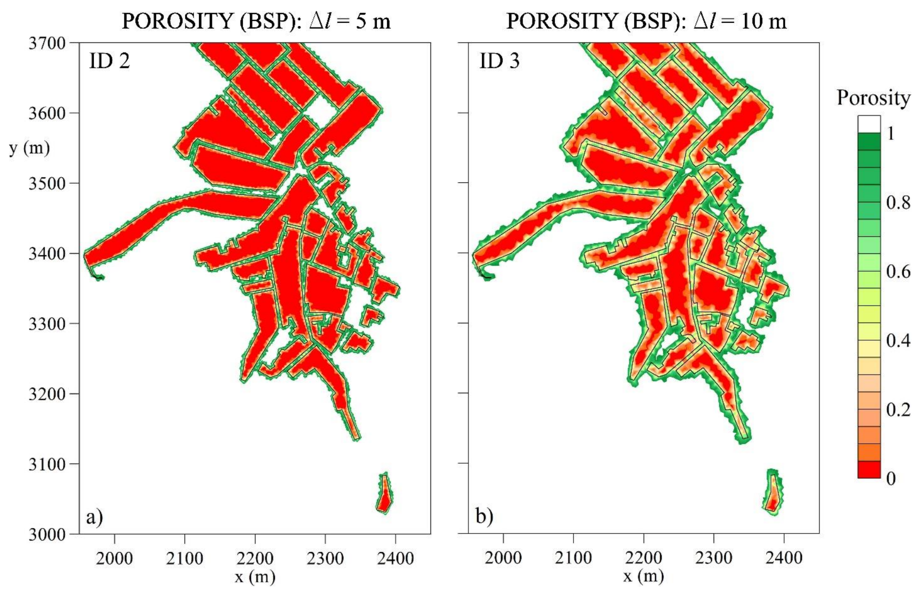

Figure 18. Tous Dam modified flood hydrograph, imposed as inflow boundary condition.

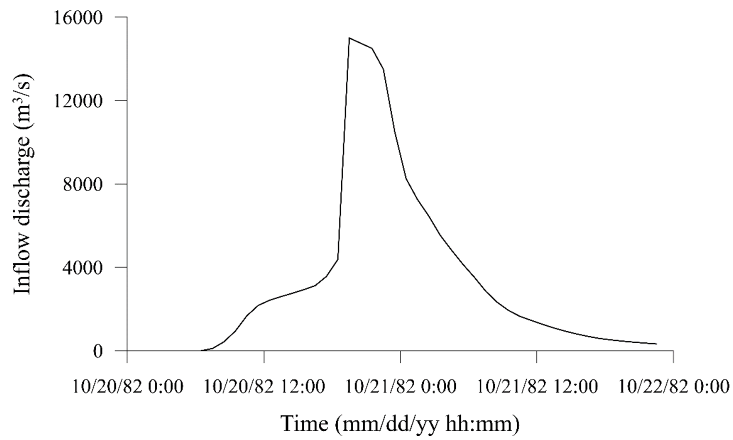

Figure 19. Tous dam-break event. Water depth (at 20:00 on October 20) for the reference simulation with resolved buildings (a), and for the porosity simulations with Δl = 5 m (b) and Δl = 10 m (c) in the city area.

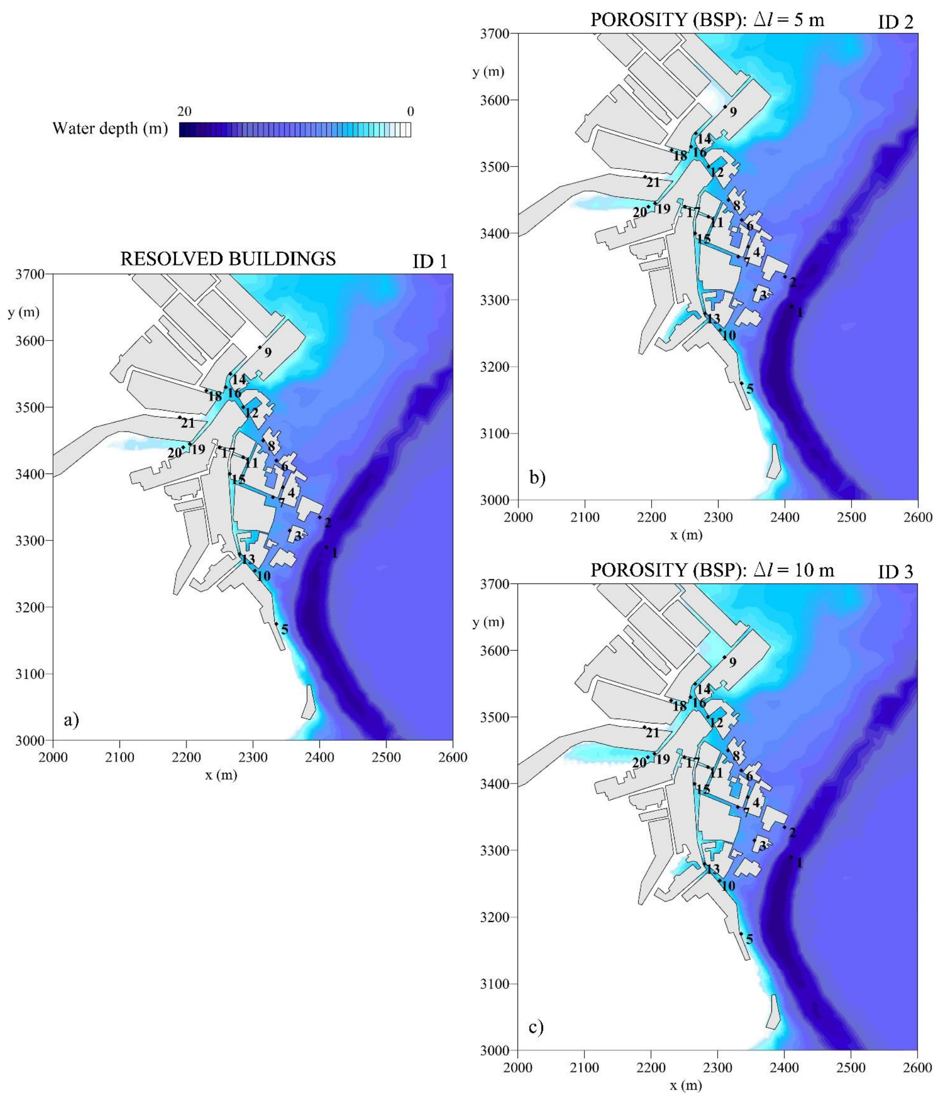

Figure 20. Tous dam-break event. Velocity fields (at 20:00 on October 20) for the reference simulation with resolved buildings (a), and for the porosity simulations with Δl = 5 m (b) and Δl = 10 m (c) in the city area.

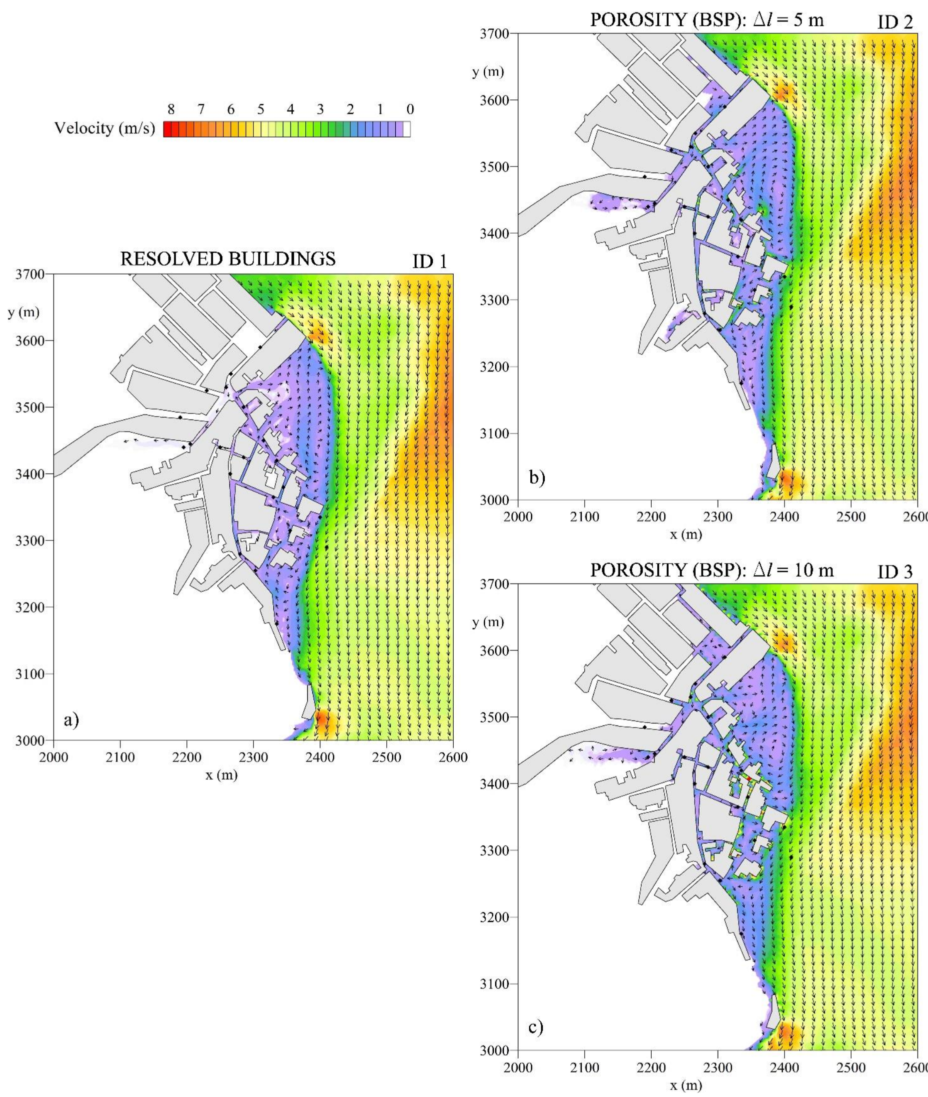

Figure 21. Tous dam-break event. Total depth (at 20:00 on October 20) for the reference simulation with resolved buildings (a), and for the porosity simulations with Δl = 5 m (b) and Δl = 10 m (c) in the city area.

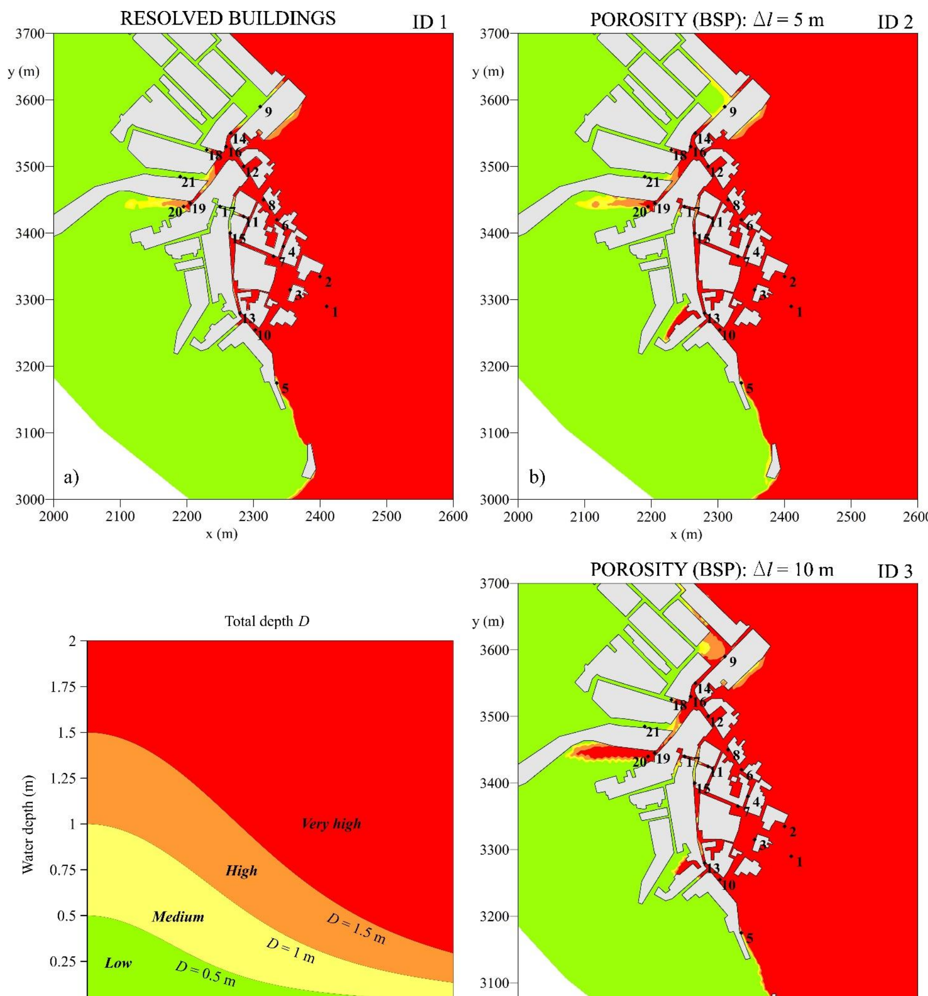

Figure 22. Tous dam-break event. Maximum water depths at gauge locations: comparison between the measured values (in black) and the results obtained by the reference model with explicitly resolved buildings (in grey), and by the porosity (BSP) model with Δl = 5 m (in white) and Δl = 10 m (in red) within the built-up area.

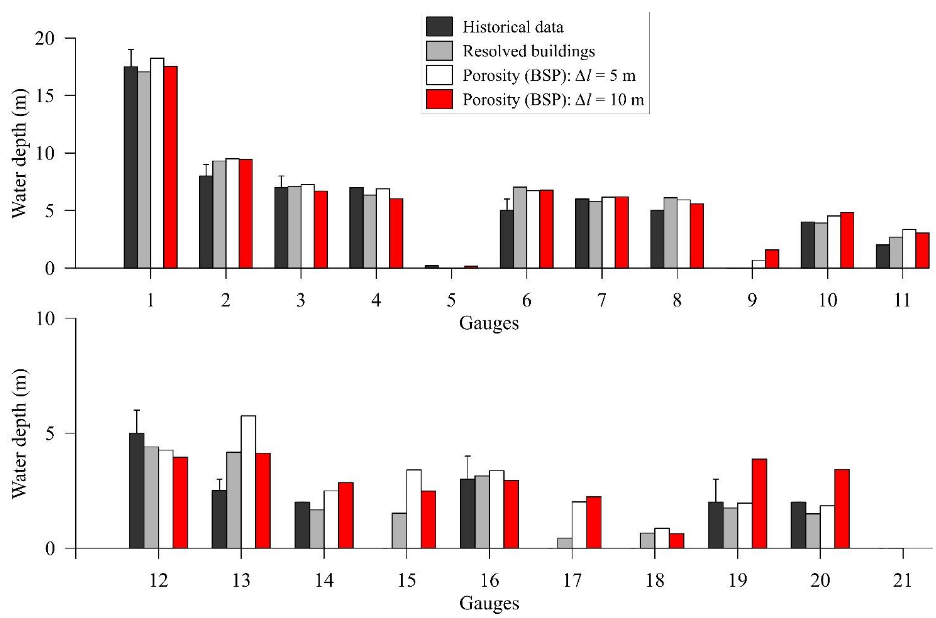

Figure 23. Speedup versus mesh ratio: experimental points (dots) and regression curve (line).